Stability and conservation properties of collocated constraints in immersogeometric fluid–thin structure interaction analysis

David Kamensky[1], John A. Evans[2], and Ming-Chen Hsu[3,*]

[1] *Center for Cardiovascular Simulation, Institute for Computational Engineering and Sciences, The University of Texas at Austin, 201 East 24th St, Stop C0200, Austin, TX 78712, USA*
[2] *Department of Aerospace Engineering Sciences, University of Colorado Boulder, 429 UCB, Boulder, CO 80309, USA*
[3] *Department of Mechanical Engineering, Iowa State University, 2025 Black Engineering, Ames, IA 50011, USA*

Abstract. The purpose of this study is to enhance the stability properties of our recently-developed numerical method [D. Kamensky, M.-C. Hsu, D. Schillinger, J.A. Evans, A. Aggarwal, Y. Bazilevs, M.S. Sacks, T.J.R. Hughes, "An immersogeometric variational framework for fluid–structure interaction: Application to bioprosthetic heart valves", Comput. Methods Appl. Mech. Engrg., 284 (2015) 1005–1053] for immersing spline-based representations of shell structures into unsteady viscous incompressible flows. In the cited work, we formulated the fluid–structure interaction (FSI) problem using an augmented Lagrangian to enforce kinematic constraints. We discretized this Lagrangian as a set of collocated constraints, at quadrature points of the surface integration rule for the immersed interface. Because the density of quadrature points is not controlled relative to the fluid discretization, the resulting semi-discrete problem may be over-constrained. Semi-implicit time integration circumvents this difficulty in the fully-discrete scheme. If this time-stepping algorithm is applied to fluid–structure systems that approach steady solutions, though, we find that spatially-oscillating modes of the Lagrange multiplier field can grow over time. In the present work, we stabilize the semi-implicit integration scheme to prevent potential divergence of the multiplier field as time goes to infinity. This stabilized time integration may also be applied in pseudo-time within each time step, giving rise to a fully implicit solution method. We discuss the theoretical implications of this stabilization scheme for several simplified model problems, then demonstrate its practical efficacy through numerical examples.

Key words: Immersogeometric analysis, fluid–structure interaction, isogeometric analysis, collocation, stabilized methods, augmented Lagrangian.

---

*Corresponding author. *Email addresses:* kamensky@ices.utexas.edu (D. Kamensky), john.a.evans@colorado.edu (J.A. Evans), jmchsu@iastate.edu (M.-C. Hsu)

The final publication is available at *Commun. Comput. Phys.* via http://doi.org/10.4208/cicp.150115.170415s

1 Introduction

The problem of thin elastic structures undergoing large, unsteady deformations while immersed in incompressible fluid has become a prominent research topic in the computational fluid–structure interaction (FSI) community. Practical instances of this problem include parachutes [1–8], insect flight [9–11], and the valves that direct blood flow through the heart [12–27]. The last topic—heart valve FSI—is currently very active: many of the cited works were published within the past several years. This intense interest is not surprising in light of the immediate practical benefits to be reaped from an improved understanding of the dynamics of both native and prosthetic heart valves.

Hundreds of thousands of diseased heart valves are surgically repaired or replaced by prostheses every year [28, 29]. The most popular type of prosthetic device is one that mimics native heart valves, consisting of thin, flexible leaflets that are pushed open by flow in one direction and pushed closed by flow in the other direction. These biomimetic devices avoid the blood damage that can be caused by mechanical prostheses consisting of rigid parts [28, 29]. To capture critical properties of soft tissue, the prostheses are often themselves composed of biologically derived materials and are hence called bioprosthetic heart valves. The durability of these valves is limited, however, and they often need to be replaced again after 10–15 years due to degradation following from repeated loading [28–30]. Attempts to design more durable prostheses would benefit from understanding the stresses that drive this degradation process. Computational methods of structural analysis have yielded some insights into the mechanics of prosthetic valves and the organs they are modeled after [31–47], but such approaches typically approximate the effect of the fluid crudely, as a uniform pressure applied to each of the valve leaflets. The goal of studies on computational heart valve FSI, such as those cited earlier, is to account for the effect of the fluid more accurately.

In our earlier work on heart valve FSI, we developed a computational method for fluid–thin structure interaction that was initially described by Kamensky et al. [27]. For reasons explained in the cited reference, we developed a non-boundary-fitted method for FSI, in which a shell structure mesh of the heart valve leaflets moves independently of a fluid background mesh. The method was later used by Hsu et al. [26] in conjunction with an arbitrary Lagrangian–Eulerian (ALE) approach [48–50] as a hybrid FSI method—a special case of the fluid–solid interface-tracking/interface-capturing technique (FSITICT) [51, 52]—to study the effect of arterial compliance on valve dynamics.

The thin shell structure in this work is discretized isogeometrically, using non-uniform rational B-spline (NURBS) basis functions [53] to represent both the geometry and the displacement solution of the structure. Hughes et al. [54] introduced isogeometric analysis (IGA) as a paradigm for expediting the tedious process of generating analysis meshes from design geometries. Aside from its potential to eliminate unnecessary labor from the design-through-analysis pipeline [55, 56], IGA has attracted a great deal of attention due to the improvements in solution quality that follow from incorporation of exact design geometry and smooth basis functions into engineering analysis [57–60]. Faithful repre-

sentations of smooth boundaries and interfaces are advantageous in the analysis of fluid mechanics [54, 61–63] and sliding contact problems [64–66], both of which are important to the dynamics of heart valves. Further, the use of smooth, spline-based analysis solution spaces can eliminate rotational degrees of freedom from thin-shell formulations, leading to simple, efficient, and robust methods for shell structure analysis [67–70].

Hughes et al. [54, page 4139] originally conceived IGA as a unification of isoparametric finite element analysis and spline-based geometrical design, as reflected through its name. An alternative means of incorporating geometry directly into analysis is to capture the geometry on an unfitted background mesh [55,71–73]. We introduced the term *immersogeometric analysis* in Kamensky et al. [27] to identify this emerging trend, and applied it to our methods for coupling isogeometric structure discretizations to fluid solutions approximated on unfitted background meshes.

In our earlier work [27], we coupled the fluid and structure through an augmented Lagrangian, integrated over the immersed interface, which we then discretized in space as a set of collocated constraints. We briefly reiterate these developments in Section 2 of the current paper. In Section 3, we modify the solution algorithm proposed by Kamensky et al. [27] to improve the stability of the discrete Lagrange multiplier field in the long-time limit. We relate this modification to the stabilization technique of Barbosa and Hughes [74] and discuss its theoretical consequences for several model problems of interest. In Section 4, we demonstrate the effects of our modified algorithm using a 2D model of a heart valve. In Section 5, we draw conclusions.

2 Augmented Lagrangian formulation for fluid–thin structure interaction

We start with the augmented Lagrangian framework for FSI introduced by Bazilevs et al. [75]. Consider space–time regions Q_1 and Q_2 (subsets of $\mathbb{R}^{d+1}$, where d is the number of spatial dimensions), occupied by incompressible Newtonian fluid and elastic solid respectively. Now define time-varying spatial domains for the fluid and structure subproblems: $(\Omega_i)_t = \{(x_1,\ldots,x_{d+1}) \in Q_i | x_{d+1} = t\}$, for $i \in \{1,2\}$. Let $(\Gamma_i)_t$ be the boundary of $(\Omega_i)_t$. $(\Omega_1)_t$ and $(\Omega_2)_t$ meet at a shared fluid–structure interface, $(\Gamma_\mathrm{I})_t$. Let $\mathbf{u}_1$ denote the fluid's velocity and p denote its pressure. Let $\mathbf{y}$ denote the structure's displacement from some reference configuration, $(\Omega_2)_0$, and $\mathbf{u}_2 \equiv \dot{\mathbf{y}}$ denote the velocity of the structure. We enforce the fluid–structure kinematic constraint that $\mathbf{u}_1 = \mathbf{u}_2$ on $(\Gamma_\mathrm{I})_t$ using the augmented Lagrangian

$$\int_{(\Gamma_\mathrm{I})_t} \boldsymbol{\lambda} \cdot (\mathbf{u}_1 - \mathbf{u}_2) \, d\Gamma + \frac{1}{2} \int_{(\Gamma_\mathrm{I})_t} \beta |\mathbf{u}_1 - \mathbf{u}_2|^2 \, d\Gamma \,, \tag{2.1}$$

where $\boldsymbol{\lambda}$ is a Lagrange multiplier and $\beta \geq 0$ is a penalty parameter. The resulting variational problem is: Find $\mathbf{u}_1 \in \mathcal{S}_u$, $p \in \mathcal{S}_p$, $\mathbf{y} \in \mathcal{S}_d$, and $\boldsymbol{\lambda} \in \mathcal{S}_\ell$ such that, for all test functions

$\mathbf{w}_1 \in \mathcal{V}_u$, $q \in \mathcal{V}_p$, $\mathbf{w}_2 \in \mathcal{V}_d$, and $\delta\boldsymbol{\lambda} \in \mathcal{V}_\ell$

$$B_1(\{\mathbf{w}_1,q\},\{\mathbf{u}_1,p\};\hat{\mathbf{u}}) - F_1(\{\mathbf{w}_1,q\}) + \int_{(\Gamma_\mathrm{I})_t} \mathbf{w}_1 \cdot \boldsymbol{\lambda}\, d\Gamma + \int_{(\Gamma_\mathrm{I})_t} \mathbf{w}_1 \cdot \beta(\mathbf{u}_1 - \mathbf{u}_2)\, d\Gamma = 0\,, \quad (2.2)$$

$$B_2(\mathbf{w}_2,\mathbf{y}) - F_2(\mathbf{w}_2) - \int_{(\Gamma_\mathrm{I})_t} \mathbf{w}_2 \cdot \boldsymbol{\lambda}\, d\Gamma - \int_{(\Gamma_\mathrm{I})_t} \mathbf{w}_2 \cdot \beta(\mathbf{u}_1 - \mathbf{u}_2)\, d\Gamma = 0\,, \quad (2.3)$$

$$\int_{(\Gamma_\mathrm{I})_t} \delta\boldsymbol{\lambda} \cdot (\mathbf{u}_1 - \mathbf{u}_2)\, d\Gamma = 0\,, \quad (2.4)$$

where $\mathcal{S}_u$, $\mathcal{S}_p$, $\mathcal{S}_d$, and $\mathcal{S}_\ell$ are the function spaces for the fluid velocity, fluid pressure, structural displacement, and Lagrange multiplier solutions, respectively, and $\mathcal{V}_u$, $\mathcal{V}_p$, $\mathcal{V}_d$, and $\mathcal{V}_\ell$ are the corresponding weighting function spaces. B_1, B_2, F_1, and F_2 are the semi-linear forms and linear functionals corresponding to the (weak) fluid and structural dynamics problems. These are defined as

$$B_1(\{\mathbf{w},q\},\{\mathbf{u},p\};\hat{\mathbf{u}}) = \int_{(\Omega_1)_t} \mathbf{w} \cdot \rho_1 \left(\left.\frac{\partial \mathbf{u}}{\partial t}\right|_{\hat{\mathbf{x}}} + (\mathbf{u} - \hat{\mathbf{u}}) \cdot \boldsymbol{\nabla}\mathbf{u} \right) d\Omega + \int_{(\Omega_1)_t} \boldsymbol{\varepsilon}(\mathbf{w}) : \boldsymbol{\sigma}_1\, d\Omega + \int_{(\Omega_1)_t} q \boldsymbol{\nabla} \cdot \mathbf{u}\, d\Omega\,, \quad (2.5)$$

$$F_1(\{\mathbf{w},q\}) = \int_{(\Omega_1)_t} \mathbf{w} \cdot \rho_1 \mathbf{f}_1\, d\Omega + \int_{(\Gamma_{1\mathbf{h}})_t} \mathbf{w} \cdot \mathbf{h}_1\, d\Gamma\,, \quad (2.6)$$

$$B_2(\mathbf{w},\mathbf{y}) = \int_{(\Omega_2)_t} \mathbf{w} \cdot \rho_2 \left.\frac{\partial^2 \mathbf{y}}{\partial t^2}\right|_{\mathbf{X}} d\Omega + \int_{(\Omega_2)_t} \boldsymbol{\varepsilon}(\mathbf{w}) : \boldsymbol{\sigma}_2\, d\Omega\,, \quad (2.7)$$

$$F_2(\mathbf{w}) = \int_{(\Omega_2)_t} \mathbf{w} \cdot \rho_2 \mathbf{f}_2\, d\Omega + \int_{(\Gamma_{2\mathbf{h}})_t} \mathbf{w} \cdot \mathbf{h}_2\, d\Gamma\,, \quad (2.8)$$

where, for $i \in \{1,2\}$, ρ_i is the mass density in $(\Omega_i)_t$, $\boldsymbol{\sigma}_i$ is the Cauchy stress, $\mathbf{f}_i$ is a prescribed body force, and $\mathbf{h}_i$ is a prescribed traction on $(\Gamma_{i\mathbf{h}})_t \subset \partial(\Omega_i)_t$. $\boldsymbol{\varepsilon}(\cdot)$ is the symmetric gradient operator, viz. $\frac{1}{2}(\boldsymbol{\nabla}(\cdot) + (\boldsymbol{\nabla}(\cdot))^T)$. We assume that $(\Omega_1)_t$ deforms from some reference configuration, $(\Omega_1)_0$, according to the velocity field $\hat{\mathbf{u}}$, which need not equal $\mathbf{u}_1$. $\partial(\cdot)/\partial t|_{\hat{\mathbf{x}}}$ indicates time differentiation with respect to a fixed point $\hat{\mathbf{x}}$ from $(\Omega_1)_0$, while $\partial(\cdot)/\partial t|_{\mathbf{X}}$ indicates time differentiation with respect to a fixed material point, $\mathbf{X}$. In this work, we assume that the fluid is Newtonian: $\boldsymbol{\sigma}_1 = -p\mathbf{I} + 2\mu\boldsymbol{\varepsilon}(\mathbf{u}_1)$, where μ is the dynamic viscosity.

In the case of a thin structure that is modeled geometrically as a surface of codimension one to $(\Omega_1)_t$ (i.e. a 2D surface for $d = 3$ or a plane curve for $d = 2$), we replace the integration over $(\Gamma_\mathrm{I})_t$ with an integral over the codimension one surface, which we refer to simply as Γ_t. For reasons expounded by Kamensky et al. [27], we eliminate the Lagrange multipliers for the tangential portion of the kinematic constraint, leaving them to be enforced by penalty only, and proceed with a scalar multiplier, λ, which enforces the no-penetration portion of the constraint. This yields the following variational problem for thin structure FSI: Find $\mathbf{u}_1 \in \mathcal{S}_u$, $p \in \mathcal{S}_p$, $\mathbf{y} \in \mathcal{S}_d$, and $\lambda \in \mathcal{S}_\ell$ such that, for all test functions

$\mathbf{w}_1 \in \mathcal{V}_u$, $q \in \mathcal{V}_p$, $\mathbf{w}_2 \in \mathcal{V}_d$, and $\delta\lambda \in \mathcal{V}_\ell$,

$$B_1(\{\mathbf{w}_1,q\},\{\mathbf{u}_1,p\};\hat{\mathbf{u}}) - F_1(\{\mathbf{w}_1,q\}) + \int_{\Gamma_t} \mathbf{w}_1 \cdot (\lambda \mathbf{n}_2)\, d\Gamma + \int_{\Gamma_t} \mathbf{w}_1 \cdot \beta(\mathbf{u}_1 - \mathbf{u}_2)\, d\Gamma = 0, \quad (2.9)$$

$$B_2(\mathbf{w}_2,\mathbf{y}) - F_2(\mathbf{w}_2) - \int_{\Gamma_t} \mathbf{w}_2 \cdot (\lambda \mathbf{n}_2)\, d\Gamma - \int_{\Gamma_t} \mathbf{w}_2 \cdot \beta(\mathbf{u}_1 - \mathbf{u}_2)\, d\Gamma = 0, \quad (2.10)$$

$$\int_{\Gamma_t} \delta\lambda \mathbf{n}_2 \cdot (\mathbf{u}_1 - \mathbf{u}_2)\, d\Gamma = 0, \quad (2.11)$$

where $\mathbf{n}_2$ is the normal to Γ_t. A formally consistent formulation could be arrived at by including terms to account for the jump in fluid viscous stresses across Γ_t (cf. Nitsche's method [76–79] and related means of weakly enforcing Dirichlet boundary conditions in fluid flow problems [80–83]), but, for discretizations considered in the present work, this jump will always be zero in the approximate solution, and has been omitted from Eqs. (2.9)–(2.11) for simplicity. Based on the relation between the augmented Lagrangian formulation with Nitsche's method, as explained by Bazilevs et al. [75], the penalty parameter should scale like

$$\beta \sim \frac{\mu}{h}\,, \quad (2.12)$$

where h has dimensions of length and is a measure of fluid mesh element size. The non-dimensional constant of proportionality is usually considered to be bounded below by element-wise inverse estimates [84–86], but, when Nitsche's method is degenerated into a pure penalty method, this is no longer a strict requirement for stability.

2.1 Semi-discrete formulation of the fluid subproblem

Galerkin's method is unstable when applied directly to the fluid subproblem Eq. (2.9). It is well known that, when advective phenomena dominate diffusion, the solution can become highly oscillatory [87, 88], and the usable combinations of discrete velocity and pressure approximation spaces are restricted by inf-sup stability considerations [89]. Further, there would be no turbulence model, and high Reynolds number flows would need to be resolved at viscous length scales. The issues of stability and turbulence modeling are simultaneously addressed by the variational multiscale (VMS) method [90] of Bazilevs et al. [91]. In short, it substitutes an ansatz for subgrid velocities and pressures into the weak fluid subproblem. This ansatz is consistent with the strong form of the Navier–Stokes equations, so that the resulting formulation smoothly transitions to direct numerical simulation as the approximation spaces are refined.

To define the mesh-dependent VMS formulation, we introduce a collection of disjoint fluid elements $\{\Omega^e\}$ such that $\Omega_1 = \cup_e \overline{\Omega^e}$. $\{\Omega^e\}$, Ω_1, and Γ remain time-dependent, but we drop the subscript t to simplify notation. We introduce a superscript h to indicate association with discrete spaces defined over these elements. The mesh $\{\Omega^e\}$ deforms with velocity $\hat{\mathbf{u}}^h$. Let $\mathcal{V}_u^h$ and $\mathcal{V}_p^h$ be discrete velocity and pressure spaces defined over

$\{\Omega^e\}$. We pose the semi-discrete VMS fluid subproblem: Find $\mathbf{u}_1^h \in \mathcal{V}_u^h$ and $p^h \in \mathcal{V}_p^h$ such that, for all $\mathbf{w}_1^h \in \mathcal{V}_u^h$ and $q^h \in \mathcal{V}_p^h$,

$$\begin{aligned} &B_1^{\text{VMS}}(\{\mathbf{w}_1^h, q^h\}, \{\mathbf{u}_1^h, p^h\}; \hat{\mathbf{u}}^h) - F_1^{\text{VMS}}(\{\mathbf{w}_1^h, q^h\}) \\ &+ \int_{\Gamma_t} \mathbf{w}_1^h \cdot (\lambda \mathbf{n}_2)\, d\Gamma + \int_{\Gamma_t} \mathbf{w}_1^h \cdot \beta(\mathbf{u}_1^h - \mathbf{u}_2)\, d\Gamma = 0\,, \end{aligned} \tag{2.13}$$

where

$$\begin{aligned} B_1^{\text{VMS}}(\{\mathbf{w}, q\}, \{\mathbf{u}, p\}; \hat{\mathbf{u}}) = &\int_{(\Omega_1)_t} \mathbf{w} \cdot \rho_1 \left(\left. \frac{\partial \mathbf{u}}{\partial t} \right|_{\hat{\mathbf{x}}} + (\mathbf{u} - \hat{\mathbf{u}}) \cdot \boldsymbol{\nabla} \mathbf{u} \right) d\Omega \\ &+ \int_{(\Omega_1)_t} \boldsymbol{\varepsilon}(\mathbf{w}) : \boldsymbol{\sigma}_1 \, d\Omega + \int_{(\Omega_1)_t} q \boldsymbol{\nabla} \cdot \mathbf{u} \, d\Omega \\ &- \sum_e \int_{\Omega^e} \left((\mathbf{u} - \hat{\mathbf{u}}) \cdot \boldsymbol{\nabla} \mathbf{w} + \frac{\boldsymbol{\nabla} q}{\rho_1} \right) \cdot \mathbf{u}' \, d\Omega \\ &- \sum_e \int_{\Omega^e} p' \boldsymbol{\nabla} \cdot \mathbf{w} \, d\Omega \\ &+ \sum_e \int_{\Omega^e} \mathbf{w} \cdot (\mathbf{u}' \cdot \boldsymbol{\nabla} \mathbf{u}) \, d\Omega \\ &- \sum_e \int_{\Omega^e} \frac{\boldsymbol{\nabla} \mathbf{w}}{\rho_1} : (\mathbf{u}' \otimes \mathbf{u}') \, d\Omega \\ &+ \sum_e \int_{\Omega^e} (\mathbf{u}' \cdot \boldsymbol{\nabla} \mathbf{w}) \overline{\tau} \cdot (\mathbf{u}' \cdot \boldsymbol{\nabla} \mathbf{u}) \, d\Omega\,, \end{aligned} \tag{2.14}$$

and

$$F_1^{\text{VMS}}(\{\mathbf{w}, q\}) = F_1(\{\mathbf{w}, q\})\,. \tag{2.15}$$

The forms $B_1^{\text{VMS}}(\cdot,\cdot)$ and $F_1^{\text{VMS}}(\cdot)$ are the VMS semi-discrete counterparts of B_1 and F_1. $\mathbf{u}'$ is the fine scale velocity ansatz,

$$\mathbf{u}' = -\tau_{\text{M}} \left(\rho_1 \left(\left. \frac{\partial \mathbf{u}}{\partial t} \right|_{\hat{\mathbf{x}}} + (\mathbf{u} - \hat{\mathbf{u}}) \cdot \boldsymbol{\nabla} \mathbf{u} - \mathbf{f} \right) - \boldsymbol{\nabla} \cdot \boldsymbol{\sigma}_1 \right)\,, \tag{2.16}$$

and p' is the fine scale pressure,

$$p' = -\rho_1 \tau_{\text{C}} \boldsymbol{\nabla} \cdot \mathbf{u}\,. \tag{2.17}$$

These clearly correspond to residuals of the strong momentum and continuity equations forming the incompressible Navier–Stokes system. The stabilization parameters τ_{M}, τ_{C}, and $\overline{\tau}$ are defined as

$$\tau_{\text{M}} = \left(s \left(\frac{4}{\Delta t^2} + (\mathbf{u} - \hat{\mathbf{u}}) \cdot \mathbf{G} (\mathbf{u} - \hat{\mathbf{u}}) + C_I \left(\frac{\mu}{\rho_1} \right)^2 \mathbf{G} : \mathbf{G} \right) \right)^{-1/2}\,, \tag{2.18}$$

$$\tau_{\text{C}} = (\tau_{\text{M}} \text{tr} \mathbf{G})^{-1}\,, \tag{2.19}$$

$$\overline{\tau} = \left(\mathbf{u}' \cdot \mathbf{G} \mathbf{u}' \right)^{-1/2}\,, \tag{2.20}$$

where Δt is a timescale associated with the as-yet-unspecified temporal discretization, C_I is a dimensionless positive constant derived from element-wise inverse estimates [84,86], and $\mathbf{G}$ generalizes the element diameter "h" to physical elements mapped through $\mathbf{x}(\boldsymbol{\xi})$ from a parametric parent element:

$$G_{ij} = \sum_{k=1}^{d} \frac{\partial \xi_k}{\partial x_i} \frac{\partial \xi_k}{\partial x_j} \,. \tag{2.21}$$

The factor s in the definition of τ_{M} is a dimensionless quantity that is allowed to vary in space. In most of Ω_1, $s = 1$, but, in an $\mathcal{O}(h)$ neighborhood of Γ, $s = s^{\mathrm{shell}} \geq 1$. This factor was introduced by Kamensky et al. [27] to improve mass conservation near the immersed structure.

Remark 2.1. The $\overline{\tau}$ term of B_1^{VMS} is not derived from VMS analysis; it is an extra term, introduced by Taylor et al. [92], to provide stabilizing dissipation near steep solution gradients.

The stabilized VMS formulation can be used with many different choices of $\mathcal{V}_u^h$ and $\mathcal{V}_p^h$. It is not limited to special inf-sup stable combinations of velocity and pressure spaces. For the computations of this paper, we use an "equal order" discretization scheme, in which the same scalar discrete space is used for pressure and each Cartesian component of velocity. This scalar space is spanned by NURBS (or B-spline) basis functions defined on d-variate parametric knot spaces. Piegl and Tiller [53] provide detailed discussion on the construction and properties of such spaces and Hughes et al. [54] review the essential components in the context of IGA.

2.2 Semi-discrete formulation of the thin structure subproblem

This section specializes the definitions of B_2 and F_2 from Eq. (2.10) to thin structures. We assume that the configuration of $(\Omega_2)_t$ is uniquely determined by Γ_t and define B_2 and F_2 as

$$B_2(\mathbf{w},\mathbf{y}) = \int_{\Gamma_t} \mathbf{w} \cdot \rho_2 h_{\mathrm{th}} \left.\frac{\partial^2 \mathbf{y}}{\partial t}\right|_{\boldsymbol{\chi}} d\Gamma + \int_{\Gamma_0} \int_{-h_{\mathrm{th}}/2}^{h_{\mathrm{th}}/2} \delta\mathbf{E} : \mathbf{S} \, d\xi_3 d\Gamma \tag{2.22}$$

and

$$F_2(\mathbf{w}) = \int_{\Gamma_t} \mathbf{w} \cdot \rho_2 h_{\mathrm{th}} \mathbf{f} \, d\Gamma + \int_{\Gamma_t} \mathbf{w} \cdot \mathbf{h}^{\mathrm{net}} \, d\Gamma \,, \tag{2.23}$$

where h_{th} is the thickness of the shell, ξ_3 is a through-thickness coordinate, and we have referred the elasticity term to the reference configuration, $(\Omega_2)_0$. $\mathbf{E}$ is the Green–Lagrange strain tensor, $\delta\mathbf{E}$ is its variation, and $\mathbf{S}$ is the second Piola–Kirchhoff stress tensor [93]. In the last term of F_2, we have summed the prescribed tractions on the two sides of Γ_t: $\mathbf{h}^{\mathrm{net}} = \mathbf{h}(\xi_3 = -h_{\mathrm{th}}/2) + \mathbf{h}(\xi_3 = +h_{\mathrm{th}}/2)$. Following Kiendl [69, Section 3.2], we simplify $\mathbf{E}$ using kinematic assumptions and define $\mathbf{S}$ through a St. Venant–Kirchhoff material model, $\mathbf{S} = \mathbb{C} : \mathbf{E}$, where $\mathbb{C}$ is an isotropic rank-four elasticity tensor, determined by a

Young's modulus, E, and Poisson ratio, ν. The integral with respect to ξ_3 can then be performed analytically [69, Eqs. (3.38) and (3.39)]. The resulting formulation [69, Eq. (3.47)] invokes second derivatives of displacement with respect to mid-surface coordinates. To directly apply Galerkin's method, we therefore need a C^1-continuous basis. Again following Kiendl [69, Chapter 5], we satisfy this requirement by using NURBS basis functions to represent displacement.

To handle structural self-contact (such as closing heart valve leaflets), we use the penalty method described by Kamensky et al. [27, Section 5.2]. In summary (and with a slight change of notation), sliding contact inequality constraints are collocated at quadrature points of the structure mid-surface and enforced by opposing pairs of penalty forces. These forces have magnitude

$$w \begin{cases} \dfrac{k_\mathrm{c}}{2h_\mathrm{c}}(d+h_\mathrm{c})^2 & , \quad d \in (-h_\mathrm{c}, 0) \\ \dfrac{k_\mathrm{c} h_\mathrm{c}}{2} + k_\mathrm{c} d & , \quad d \geq 0 \\ 0 & , \quad \text{otherwise} \end{cases} , \tag{2.24}$$

where w is the weight of the quadrature point at which the constraint is collocated, d is the (signed) depth of penetration, k_c is the contact penalty parameter, and h_c is the length over which activation of penalty forces is smoothed, to improve nonlinear convergence. Penetrations of $|d| > c_\mathrm{c}$ are ignored, where $c_\mathrm{c} \geq h_\mathrm{c}$ is a cutoff to avoid spurious non-local contact. Weighting the penalty forces by a quadrature rule ensures that parallel plates will always experience a uniform pressure.

2.3 Spatial discretization of the FSI constraints

To numerically perform the integrals over Γ_t, we introduce a quadrature rule on Γ_t that consists of a summation over Gaussian quadrature rules on disjoint elements of Γ_t. In all computations from this paper, these quadrature rules are the same ones used to integrate the structure subproblem formulated in Section 2.2, but this coincidence is not necessary. We recommend that the size of the surface quadrature elements be bounded above by some measure of the fluid mesh element size, although this is not strictly enforced by the formulation.

The integration of the penalty terms is then straightforward: $\mathbf{u}_2^h$ may be evaluated directly at the surface quadrature point, and the parameterization of the fluid element containing the quadrature point's spatial location may be inverted to obtain parametric coordinates at which to evaluate $\mathbf{u}_1^h$. The number of fluid elements in which this parametric inversion must be attempted for each quadrature point can be greatly reduced by using techniques from computational geometry. Some problems may benefit from splitting the penalty force into normal and tangential components, which may be weighted

separately [75]. This is accomplished by replacing

$$\beta\left(\mathbf{u}_1^h - \mathbf{u}_2^h\right) \tag{2.25}$$

with

$$\left(\tau_{\text{NOR}}^B - \tau_{\text{TAN}}^B\right)\left(\left(\mathbf{u}_1^h - \mathbf{u}_2^h\right)\cdot\mathbf{n}_2\right)\mathbf{n}_2 + \tau_{\text{TAN}}^B\left(\mathbf{u}_1^h - \mathbf{u}_2^h\right), \tag{2.26}$$

where τ_{NOR}^B and τ_{TAN}^B are the normal and tangential penalties.

Remark 2.2. Recall that Eq. (2.12) is merely a *lower* bound on these penalties. It is not entirely satisfactory for τ_{NOR}^B to be proportional to μ, since this implies that penalization of fluid penetration through the structure will vanish in the inviscid limit. In the numerical examples of this paper, we proceed with $\tau_{\text{NOR}}^B \sim \mu/h$, which is effective for low to moderate Reynolds numbers. We anticipate that some other means of selecting τ_{NOR}^B would be necessary for $Re \gg 1$ if we wish to avoid a situation in which users must carefully choose the non-dimensional penalty constant through numerical experiments, but the development of a precise formula applicable to singularly perturbed problems is beyond the scope of the present work.

To integrate the multiplier term, we must have a way of evaluating the multiplier field at quadrature points of Γ_t. To this end, we simply introduce a scalar unknown at each surface quadrature point, which is interpreted as the value of λ at that point. This corresponds to collocation of the no-penetration constraint at the quadrature points.

3 Fully-discrete formulation

In this section, we complete the discretization by specifying a time-marching procedure. We will compute approximate solutions at a countable set of time levels, indexed by n and separated in time by steps of size Δt. Suppose that, at time level n, the discrete fluid velocity is defined by a vector of coefficients $\mathbf{U}^n$, the fluid acceleration by $\dot{\mathbf{U}}^n$, the fluid pressure by $\mathbf{P}^n$, and the structure displacement, velocity, and acceleration by $\mathbf{Y}^n$, $\dot{\mathbf{Y}}^n$, and $\ddot{\mathbf{Y}}^n$, respectively. We refer to the multiplier at time level n as λ^n, considering it a function defined over Γ_t, with the understanding that it is represented discretely as a set of samples at quadrature points. Considering the solution variables at time level n known, we first construct a system of equations for all $(n+1)$-level unknowns, excluding λ^{n+1}, which we initially set equal to λ^n:

$$\text{Res}\left(\mathbf{U}^{n+\alpha_f}, \dot{\mathbf{U}}^{n+\alpha_m}, \mathbf{Y}^{n+\alpha_f}, \dot{\mathbf{Y}}^{n+\alpha_f}, \ddot{\mathbf{Y}}^{n+\alpha_m}, \mathbf{P}^{n+1}, \lambda^{n+1}\right) = \mathbf{0}, \tag{3.1}$$

$$\mathbf{U}^{n+1} = \mathbf{U}^n + \Delta t\left((1-\gamma)\dot{\mathbf{U}}^n + \gamma\dot{\mathbf{U}}^{n+1}\right), \tag{3.2}$$

$$\dot{\mathbf{U}}^{n+\alpha_m} = \dot{\mathbf{U}}^n + \alpha_m\left(\dot{\mathbf{U}}^{n+1} - \dot{\mathbf{U}}^n\right), \tag{3.3}$$

$$\mathbf{U}^{n+\alpha_f} = \mathbf{U}^n + \alpha_f\left(\mathbf{U}^{n+1} - \mathbf{U}^n\right), \tag{3.4}$$

$$\mathbf{Y}^{n+1} = \mathbf{Y}^n + \Delta t \dot{\mathbf{Y}}^n + \frac{\Delta t^2}{2}\left((1-2\beta)\ddot{\mathbf{Y}}^n + 2\beta\ddot{\mathbf{Y}}^{n+1}\right), \tag{3.5}$$

$$\dot{\mathbf{Y}}^{n+1} = \dot{\mathbf{Y}}^n + \Delta t\left((1-\gamma)\ddot{\mathbf{Y}}^n + \gamma\ddot{\mathbf{Y}}^{n+1}\right), \tag{3.6}$$

$$\ddot{\mathbf{Y}}^{n+\alpha_m} = \ddot{\mathbf{Y}}^n + \alpha_m\left(\ddot{\mathbf{Y}}^{n+1} - \ddot{\mathbf{Y}}^n\right), \tag{3.7}$$

$$\dot{\mathbf{Y}}^{n+\alpha_f} = \dot{\mathbf{Y}}^n + \alpha_f\left(\dot{\mathbf{Y}}^{n+1} - \dot{\mathbf{Y}}^n\right), \tag{3.8}$$

$$\mathbf{Y}^{n+\alpha_f} = \mathbf{Y}^n + \alpha_f\left(\mathbf{Y}^{n+1} - \mathbf{Y}^n\right), \tag{3.9}$$

where α_m, α_f, β, and γ are parameters of the time integration scheme. The function $\mathrm{Res}(\ldots)$ is the nonlinear residual corresponding to the discretization of Eqs. (2.9) and (2.10). Note that this does not include the FSI kinematic constraint equation (2.11), which, because λ^{n+1} is held fixed, would lead to an ill-posed system with more equations than unknowns. While the multiplier is considered fixed in this problem, the penalty terms are still treated implicitly. We solve this penalty-coupled problem by block iteration, as described by Kamensky et al. [27, Section 4.6]. The formulas (3.1)–(3.9) are based on the generalized-α method of time integration [94]. Following Bazilevs et al. [95, Section 4.4], we work within a subset of generalized-α methods, parameterized by as single scalar, $\rho_\infty \in [0,1]$, which controls numerical damping and defines the four free parameters as

$$\alpha_m = \frac{1}{2}\left(\frac{3-\rho_\infty}{1+\rho_\infty}\right), \tag{3.10}$$

$$\alpha_f = \frac{1}{1+\rho_\infty}, \tag{3.11}$$

$$\gamma = \frac{1}{2} + \alpha_m - \alpha_f, \tag{3.12}$$

$$\beta = \frac{1}{4}\left(1+\alpha_m+\alpha_f\right)^2. \tag{3.13}$$

For all computations in this paper, we use $\rho_\infty = 0.5$. For a discussion of the effects of this parameter on stabilized finite element computations of unsteady Navier–Stokes, see the work of Jansen et al. [96].

Remark 3.1. A more canonical implementation of the generalized-α scheme might introduce

$$\lambda^{n+\alpha_f} = \lambda^n + \alpha_f\left(\lambda^{n+1} - \lambda^n\right) \tag{3.14}$$

and

$$\mathbf{P}^{n+\alpha_f} = \mathbf{P}^n + \alpha_f\left(\mathbf{P}^{n+1} - \mathbf{P}^n\right) \tag{3.15}$$

for use in Eq. (3.1), but the formulation has no time derivatives of the corresponding fields,[†] and their α-level coefficients would be uniquely determined by the fully-discrete

[†]In Section 3.2, we reinterpret the algorithm developed in this section as taking a time derivative of λ, but we consider this to be a *post hoc* interpretation of the discrete scheme for stability analysis, not a statement of the formulation itself.

formulation, leaving Eqs. (3.14) and (3.15) as post-processing steps for the $(n+1)$-level unknowns. We follow Bazilevs et al. [91] in simply renaming these α-level unknowns to $(n+1)$-level unknowns. This has no effect on the values of the fluid velocity and structure displacement coefficients and essentially translates the pressure and multiplier solutions by a fraction of Δt in time.

Because Eqs. (3.1)–(3.9) do not include the constraint given by Eq. (2.11), the α-level constraint residual

$$R^{n+\alpha} = \left(\left(\mathbf{u}_1^h \right)^{n+\alpha_f} - \left(\mathbf{u}_2^h \right)^{n+\alpha_f} \right) \cdot \mathbf{n}_2^{n+\alpha_f} \tag{3.16}$$

is not necessarily zero on $\Gamma_{t+\alpha_f}$. In Eq. (3.16), $\left(\mathbf{u}_1^h \right)^{n+\alpha_f}$ is the fluid velocity defined by coefficients $\mathbf{U}^{n+\alpha_f}$, $\left(\mathbf{u}_2^h \right)^{n+\alpha_f}$ is the structure velocity defined by coefficients $\dot{\mathbf{Y}}^{n+\alpha_f}$, and $\mathbf{n}_2^{n+\alpha_f}$ is the normal to $\Gamma_{t+\alpha_f}$, as determined by the displacement coefficients $\mathbf{Y}^{n+\alpha_f}$.

If $R^{n+\alpha} = 0$, then the normal component of the α-level penalty force, $\tau_{\text{NOR}}^B R^{n+\alpha}$, will be zero and the normal α-level fluid–structure force will be due only to the Lagrange multiplier, λ^{n+1}. This motivates the explicit update

$$\lambda^{n+1} \leftarrow \lambda^{n+1} + \tau_{\text{NOR}}^B R^{n+\alpha} \,, \tag{3.17}$$

in which λ^{n+1} is set equal to the α-level fluid–structure forcing. Eqs. (3.1)–(3.9) are of course no longer satisfied with the updated λ^{n+1}, but we may attempt to iterate the steps

1. Solve Eqs. (3.1)–(3.9) with λ^{n+1} fixed.

2. Upate λ^{n+1} by Eq. (3.17).

until $\| R^{n+\alpha} \|_{L^2(\Gamma_t)}$ is converged to some tolerance. As explained by Kamensky et al. [27, Section 4.2.1], this iteration corresponds to the classic augmented Lagrangian algorithm of Hestenes [97] and Powell [98], which is an implicit variant of the well-known Uzawa iteration [99, 100] for solving saddle point problems. In the present case, though, the convergence criterion of $\| R^{n+\alpha} \|_{L^2(\Gamma_t)} < \epsilon$ is too strict to arrive at a nontrivial solution; it effectively demands pointwise constraint satisfaction between the non-matching discrete velocity spaces of the fluid and structure. Kamensky et al. [27] found accordingly that the iteration did not typically converge, but circumvented this difficulty by truncating to a single pass, leading to the semi-implicit time marching scheme of first solving Eqs. (3.1)–(3.9) with $\lambda^{n+1} = \lambda^n$, then updating λ^{n+1} by Eq. (3.17) and continuing directly to the next time step. This time splitting approach proved effective for transient problems, but may be expected to run into difficulties in problems that approach steady solutions.

In the present work, we alter the discrete constraint residual to be

$$R^{n+\alpha} = \left(\left(\mathbf{u}_1^h \right)^{n+\alpha_f} - \left(\mathbf{u}_2^h \right)^{n+\alpha_f} \right) \cdot \mathbf{n}_2^{n+\alpha_f} - \left(\frac{r}{\tau_{\text{NOR}}^B} \right) \lambda^{n+1} \,, \tag{3.18}$$

where $r \geq 0$ is a parameter. If τ^B_{NOR} is considered to scale inversely with h, as in Eq. (2.12), this adds some $\mathcal{O}(h)$ leeway into the convergence criterion for the constraint equation. If we consider λ^{n+1} in Eq. (3.18) to be the updated multiplier on the left side of the assignment in Eq. (3.17), then the update given by Eq. (3.17) becomes implicit, but it may trivially be recast into the explicit form

$$\lambda^{n+1} \leftarrow \frac{\lambda^{n+1} + \tau^B_{\text{NOR}} \left(\left(\mathbf{u}_1^h \right)^{n+\alpha_f} - \left(\mathbf{u}_2^h \right)^{n+\alpha_f} \right) \cdot \mathbf{n}_2^{n+\alpha_f}}{1+r} \,. \tag{3.19}$$

This reduces to our earlier algorithm when $r=0$. In the continuous problem, the modification to the constraint residual corresponds to a stabilized formulation of Eqs. (2.9)–(2.11), in which the constraint equation (2.11) is repaced by

$$\int_{\Gamma_t} \delta\lambda \left(\left(\mathbf{u}_1^h - \mathbf{u}_2^h \right) \cdot \mathbf{n}_2 - \left(\frac{r}{\beta} \right) \lambda \right) \, d\Gamma \, = \, 0 \,. \tag{3.20}$$

Eq. (3.20) represents a degenerate case of Barbosa–Hughes stabilization [74,101]. It could be rendered formally consistent with the exact solution by subtracting the pressure jump across Γ_t from λ in the stabilization term, but, in the present case, the pressure jump in the discrete solution is zero and we have simply omitted it from Eq. (3.20). Section 3.1 provides some insight into the effects of this *de facto* consistency error.

Although stabilization affords the possibility of fully-implicit time integration, which is typically recommended for complex FSI problems [102], semi-implicit integration procedures can greatly reduce computational cost. In the present work, we generalize our earlier semi-implicit scheme to use the stabilized update formula (3.19). In Section 3.2, we show that the generalized semi-implicit scheme is stable (in an energetic sense) when applied to simplified linear model problems, even when $r=0$, in contrast to "staggered" or "loosely coupled" FSI methods which are notoriously unstable, especially when the fluid is incompressible [103], prompting widespread preference for implicit methods. Our earlier computations [26,27] and the numerical examples in Section 4 of this paper indicate that the energy stability results extrapolate well to the fully nonlinear FSI problem. The use of $r>0$ allows for robustness even when energy is continuously added to the system, as through an inhomogeneous boundary condition.

3.1 Analysis of plug flow

To get a rough intuition of how the stabilization introduced in Section 3 affects solutions, we introduce the simple model of plug flow through a blocked tube: a rigid barrier cuts across a channel filled with a fluid that we assume, *a priori*, to have a single velocity, $u\mathbf{e}_1$, that is constant across space, but may vary with time. To allow nonzero velocity solutions with this kinematic assumption, we apply slip boundary conditions on the channel walls. This is illustrated in Figure 1.

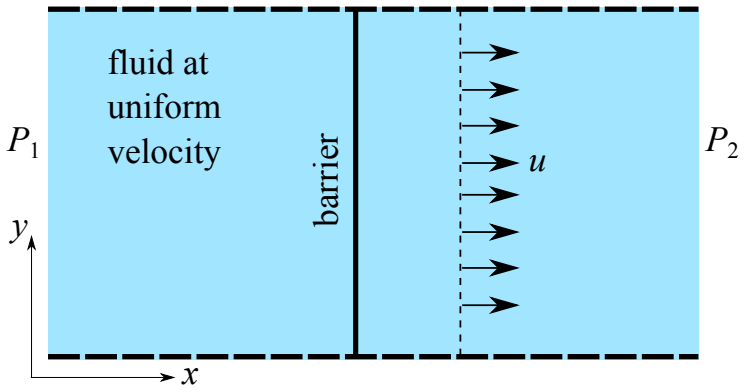

Figure 1: Plug flow through a tube, blocked by a barrier. In the exact solution, u must be zero, but weak enforcement techniques can allow leakage.

3.1.1 Leakage

Suppose that the ends of the channel are subject to pressures P_1 and P_2, which define the pressure drop, $\Delta P = P_1 - P_2$. Suppose also, for now, that the Lagrange multiplier field takes on a single constant value across the barrier. Then the steady state solution of the semi-implicit time integration procedure described in Section 3 will reduce to the conditions

1. Steadiness: $\lambda^{n+1} = \lambda^n$. We define this constant value to be λ^∞, and it must satisfy $\lambda^\infty = \left(\lambda^\infty + \tau^B_{\text{NOR}} u\right) / (1+r)$.

2. Equilibrium: $\lambda + \tau^B_{\text{NOR}} u = \Delta P$; the multiplier and penalty must balance the pressure drop to preclude acceleration of the fluid plug.

It follows that the leakage, u, is given by

$$u = \frac{r \Delta P}{\tau^B_{\text{NOR}} (1+r)} \,, \tag{3.21}$$

which asymptotes to inverse scaling with the penalty parameter as $r \to \infty$ and to zero as $r \to 0$. For a fixed nonzero value of r, we then have that leakage converges to zero with refinement at the same rate as it would for a pure penalty method, but, if we consider r to be an adjustable parameter, we may scale the leakage down to arbitrarily small levels without impacting the solvability of the discrete problem at each time step (because r appears only in the explicit multiplier update).

3.1.2 Spurious modes of λ

If we allow λ to vary across the cross-section of the pipe, it is immediately clear that there are many choices which could satisfy the equilibrium condition. Any λ with $\int_\Gamma \lambda \, d\Gamma = 0$

could be added to an existing solution and corresponds to a "spurious mode" of the Lagrange multiplier field. Such modes will exist for richer fluid approximation spaces as well. Any λ that is L^2-orthogonal to the discrete space of fluid–structure velocity differences will constitute such a spurious mode. Our solution algorithm explicitly constructs the multiplier approximation as a linear combination of discrete fluid–structure velocity differences, and is therefore, in principle, immune to such spurious modes. In practice, though, we find that the multiplier field can develop oscillations that are *nearly* orthogonal to the space of velocity differences. Without stabilization, they may become quite large, as demonstrated by the numerical experiments of Section 4. The analysis of Section 3.2 indicates that these oscillations may be viewed as storing energy, which can later be unleashed into the fluid and structure sub-problems; if oscillations in λ grow to extreme magnitudes, the subsequent release of energy could be catastrophic.

3.1.3 Conflicting boundary conditions

If a Dirichlet condition is applied to the plug flow, constraining u to have some nonzero value, then, when $r=0$, λ will clearly diverge as $t\to\infty$. This corresponds, of course, to an ill-posed problem with contradictory boundary conditions, but such situations may be approached in practice, if, for instance, the structure is forced into a fluid element whose nodes are subject to Dirichlet boundary conditions. When $r>0$, the semi-implicit time integration remains robust in this extreme limit: assuming again that λ takes on a single value across the barrier, the steadiness condition, $\lambda^\infty=\left(\lambda^\infty+\tau^B_{\mathrm{NOR}}u\right)/(1+r)$ implies that λ stabilizes at a value of $\tau^B_{\mathrm{NOR}}u/r$ as $t\to\infty$.

3.2 Energy analysis of the semi-implicit scheme

To assess the stability of the semi-implicit time integration scheme, we relate it to a fully-implicit integration of a surrogate problem. Kamensky et al. [27, Section 4.2.1] made such a comparison earlier, for the case of $r=0$, showing that the semi-implicit update algorithm for the multiplier was equivalent to replacing the multiplier and penalty forces by an implicitly treated forcing due to a field λ satisfying the auxiliary differential equation $\dot\lambda=\left(\tau^B_{\mathrm{NOR}}/\Delta t\right)\left(\mathbf{u}^h_1-\mathbf{u}^h_2\right)\cdot\mathbf{n}_2$, integrated with the backward Euler algorithm at each material point of the structure mid-surface. For $r\geq 0$, we can straightforwardly generalize this surrogate problem to have a fluid–structure forcing $(1+r)\lambda$, with λ satisfying

$$\dot\lambda=\left(\tau^B_{\mathrm{NOR}}/\Delta t\right)\left(\mathbf{u}^h_1-\mathbf{u}^h_2\right)\cdot\mathbf{n}_2-(r/\Delta t)\lambda \tag{3.22}$$

at each material point of the structure mid-surface. Discretizing (3.22) using the backward Euler method, we obtain

$$\frac{\lambda^{n+1}-\lambda^n}{\Delta t}=\left(\tau^B_{\mathrm{NOR}}/\Delta t\right)\left(\left(\mathbf{u}^h_1\right)^{n+\alpha_f}-\left(\mathbf{u}^h_2\right)^{n+\alpha_f}\right)\cdot\mathbf{n}_2-(r/\Delta t)\lambda^{n+1}\,, \tag{3.23}$$

where we recall Remark 3.1, which explains how we consider the $(n+1)$-level multiplier unknowns to be coincident in time with the $(n+\alpha_f)$-level velocities. Multiplying Eq. (3.23) by Δt and rearranging terms, we recover the explicit update formula

$$\lambda^{n+1} = \frac{\lambda^n + \tau^B_{\mathrm{NOR}} \left(\left(\mathbf{u}_1^h\right)^{n+\alpha_f} - \left(\mathbf{u}_2^h\right)^{n+\alpha_f} \right) \cdot \mathbf{n}_2}{1+r} \,, \tag{3.24}$$

which is equivalent to Eq. (3.19) in the case of the semi-implicit algorithm. Multiplying Eq. (3.24) by $(1+r)$, we see that the α-level fluid–structure pressure in the semi-implicit scheme,

$$\lambda^n + \tau^B_{\mathrm{NOR}} \left(\left(\mathbf{u}_1^h\right)^{n+\alpha_f} - \left(\mathbf{u}_2^h\right)^{n+\alpha_f} \right) \cdot \mathbf{n}_2 \,, \tag{3.25}$$

is equal to $(1+r)\lambda^{n+1}$, which is the $(n+1)$-level fluid–structure pressure in our implicitly-integrated surrogate problem. The semi-implicit algorithm is therefore equivalent to fully implicit integration of a surrogate problem in which the fluid–structure pressure is $(1+r)\lambda$ and λ solves Eq. (3.22).

The inverse dependence of the coefficients of Eq. (3.22) on Δt interferes with convergence analysis. We do not claim that the semi-implicit scheme computes a λ that accurately solves Eq. (3.22). We introduce Eq. (3.22) as a device to study *stability*. An unconditionally stable time integration scheme will inherit the stability properties of the underlying time-continuous problem for all time steps, including those that happen to be related to the coefficients of the continuous problem.

To investigate the stability of this surrogate semidiscrete problem, we now consider its application to the simplified model of a linearized fluid problem (e.g. unsteady Stokes or Oseen flow) interacting with a small-deformation elastodynamic thin structure problem. We anticipate that the following discussion could extend to the nonlinear setting by invoking the linear stability of the VMS formulation with grad-div stabilization [104, Chapter 3]. We pose the fluid subproblem on Ω_1 and the structure subproblem on the codimension-one surface $\Gamma \subset \Omega_1$. Ω_1 and Γ are assumed to be independent of time, in keeping with the restriction to small deformation theory. We assume that the fluid subproblem is of the form: Find a semidiscrete velocity and pressure pair $\left\{\mathbf{u}_1^h, p^h\right\} \in \mathcal{V}_u^h \times \mathcal{V}_p^h$ such that, $\forall \left\{\mathbf{w}_1^h, q^h\right\} \in \mathcal{V}_u^h \times \mathcal{V}_p^h$,

$$\left(\rho_1 \partial_t \mathbf{u}_1^h, \mathbf{w}_1^h\right)_{L^2(\Omega_1)} + b_1\left(\left\{\mathbf{u}_1^h, p^h\right\}, \left\{\mathbf{w}_1^h, q^h\right\}\right) = f_1\left(\left\{\mathbf{w}_1^h, q^h\right\}\right) \,, \tag{3.26}$$

where we assume that the solution $\left\{\mathbf{u}_1^h, p^h\right\}$ exists and that $b_1\left(\left\{\mathbf{u}_1^h, p^h\right\}, \left\{\mathbf{u}_1^h, p^h\right\}\right) \geq 0$. The second assumption would follow immediately from coercivity of $b_1(\cdot,\cdot)$, but it does not, in general, require coercivity. It will be satisfied, for instance, by Galerkin's method applied to Stokes flow, or Oseen flow with homogeneous Dirichlet boundary conditions on $\partial\Omega_1$. We employ the superscript $(\cdot)^h$ to emphasize that results hold after discretizing in space, but we do not rely in any way on $\mathcal{V}_{(\cdot)}^h$ having finite dimension. Inserting the

solution as a test function,

$$\partial_t\left(\frac{1}{2}\rho_1\left\|\mathbf{u}_1^h\right\|^2_{L^2(\Omega_1)}\right)=f_1\left(\left\{\mathbf{u}_1^h,p^h\right\}\right)-b_1\left(\left\{\mathbf{u}_1^h,p^h\right\},\left\{\mathbf{u}_1^h,p^h\right\}\right)\leq f_1\left(\left\{\mathbf{u}_1^h,p^h\right\}\right)\ . \quad (3.27)$$

Suppose that

$$f_1\left(\left\{\mathbf{w}_1^h,q^h\right\}\right)=-(1+r)\int_\Gamma\lambda\left(\mathbf{w}_1^h\cdot\mathbf{n}\right)\,d\Gamma\ . \quad (3.28)$$

Then we may interpret inequality (3.27) as saying that the rate of change in kinetic energy of the semi-discrete solution $\mathbf{u}_1^h$ is bounded by the rate of work done by the surface force $-(1+r)\lambda\mathbf{n}$.

Likewise define the structure subproblem as: Find a displacement $\mathbf{y}^h\in\mathcal{V}_y^h$ such that, $\forall\mathbf{w}_2^h\in\mathcal{V}_y^h$,

$$\left(\rho_2\partial_t^2\mathbf{y}^h,\mathbf{w}_2^h\right)_{L^2(\Gamma)}+a_2(\mathbf{y}^h,\mathbf{w}_2^h)+b_2\left(\partial_t\mathbf{y}^h,\mathbf{w}_2^h\right)=f_2\left(\mathbf{w}_2^h\right)\ , \quad (3.29)$$

where we again assume that the problem is well-posed, $a_2(\cdot,\cdot)$ is a bilinear symmetric positive-definite form providing elasticity, and $b_2(\cdot,\cdot)$ is a damping form that satisfies $b_2(\partial_t\mathbf{y}^h,\partial_t\mathbf{y}^h)\geq 0$. Let

$$f_2\left(\mathbf{w}_2^h\right)=(1+r)\int_\Gamma\lambda\left(\mathbf{w}_2^h\cdot\mathbf{n}\right)\,d\Gamma\ , \quad (3.30)$$

where λ is the same quantity used in defining $f_1(\cdot)$. Define the semidiscrete potential energy as

$$\Psi^h=\frac{1}{2}a_2\left(\mathbf{y}^h,\mathbf{y}^h\right)\ . \quad (3.31)$$

Mild regularity assumptions on $a_2(\cdot,\cdot)$ and $\mathbf{y}^h$ imply the time derivative product rule

$$\partial_t a_2\left(\mathbf{y}^h,\mathbf{y}^h\right)=a_2\left(\partial_t\mathbf{y}^h,\mathbf{y}^h\right)+a_2\left(\mathbf{y}^h,\partial_t\mathbf{y}^h\right)=2a_2\left(\mathbf{y}^h,\partial_t\mathbf{y}^h\right)\ . \quad (3.32)$$

Inserting $\mathbf{u}_2^h\equiv\partial_t\mathbf{y}^h$ as the test function $\mathbf{w}_2^h$ in the structure subproblem, we then find that the rate of change of combined kinetic and potential energy in the structure subproblem is bounded by interface power:

$$\partial_t\left(\frac{1}{2}\rho_2\left\|\mathbf{u}_2^h\right\|^2_{L^2(\Gamma)}+\Psi^h\right)\leq(1+r)\int_\Gamma\lambda\left(\mathbf{u}_2^h\cdot\mathbf{n}\right)\,d\Gamma\ . \quad (3.33)$$

Suppose that, at each point $\mathbf{x}\in\Gamma$, the interface pressure $(1+r)\lambda(\mathbf{x},t)$ is determined by solving the differential equation

$$\partial_t\lambda(\mathbf{x},t)=k\left(\mathbf{u}_1^h(\mathbf{x},t)-\mathbf{u}_2^h(\mathbf{x},t)\right)\cdot\mathbf{n}(\mathbf{x})-c\lambda(\mathbf{x},t)\ , \quad (3.34)$$

where $k=\tau^B_{\mathrm{NOR}}/\Delta t$, $c=r/\Delta t$, and $\mathbf{n}$ is the normal to Γ. Then, defining $u\equiv\left(\mathbf{u}_1^h-\mathbf{u}_2^h\right)\cdot\mathbf{n}$ and multiplying by the integrating factor e^{ct},

$$e^{ct}\left(\partial_t\lambda\right)+ce^{ct}\lambda=kue^{ct} \tag{3.35}$$

$$\Rightarrow\ \partial_t\left(e^{ct}\lambda\right)=kue^{ct} \tag{3.36}$$

$$\Rightarrow\ e^{ct}\lambda=k\int_0^t ue^{c\tau}d\tau \tag{3.37}$$

$$\Rightarrow\ \lambda=e^{-ct}k\int_0^t ue^{c\tau}d\tau\ , \tag{3.38}$$

where we have assumed that $\lambda=0$ at time $t=0$. The net work per unit area done after time t by the multiplier on the combined fluid–structure system is given by

$$\begin{aligned} w(t)&=-(1+r)\int_0^t\lambda(\mathbf{x},\tau)u(\mathbf{x},\tau)\ d\tau \\ &=-(1+r)k\int_0^t u(\mathbf{x},\tau)\left\{e^{-c\tau}\int_0^\tau u(\mathbf{x},T)e^{cT}\ dT\right\}\ d\tau\ . \end{aligned} \tag{3.39}$$

Define

$$g(\tau)\equiv e^{-c\tau}\int_0^\tau ue^{cT}\ dT\ . \tag{3.40}$$

Then

$$\partial_\tau g=-ce^{-c\tau}\int_0^\tau ue^{cT}\ dT+e^{-c\tau}ue^{c\tau} \tag{3.41}$$

$$=-ce^{-c\tau}\int_0^\tau ue^{cT}\ dT+u\ , \tag{3.42}$$

and

$$g\partial_\tau g=-c\left(e^{-c\tau}\int_0^\tau ue^{cT}\ dT\right)^2+ue^{-c\tau}\int_0^\tau ue^{cT}\ dT\ . \tag{3.43}$$

Then

$$w(t)=-(1+r)k\int_0^t\left\{g\partial_t g+c\left(e^{-c\tau}\int_0^\tau ue^{cT}\ dT\right)^2\right\} \tag{3.44}$$

$$=-(1+r)k\left\{\int_0^t\frac{1}{2}\partial_\tau\left(g^2\right)\ d\tau+\int_0^t\left(c\left(e^{-c\tau}\int_0^\tau ue^{cT}\ dT\right)^2\right)\ d\tau\right\} \tag{3.45}$$

$$\leq-(1+r)\frac{1}{2}kg^2\leq 0\ . \tag{3.46}$$

Integrating inequalities (3.27) and (3.33) with respect to time, we see that the sum of the kinetic energy of the fluid–structure system and the potential energy of the structure

changes by at most $\int_\Gamma w(\mathbf{x},t)\ d\mathbf{x}$, which is non-positive. The combined energy is therefore bounded by its initial value. The non-negativity of the kinetic and potential energy functionals implies that they remain individually bounded for all time. The semidiscrete coupled problem therefore has an L^2-stable fluid velocity solution and a structure displacement solution with bounded internal energy.

The above discussion does not specify a discretization of the field λ. Assuming C^0-continuous discrete fluid velocity and structure displacement spaces, the surface integration measure $d\Gamma$ could be replaced by a weighted sum of Dirac measures, corresponding to the (inexact) quadrature rule described in Section 2.3, and these energy stability results would remain true. Penalization of velocity difference, which we use to enforce no-slip constraints on thin structures, is purely dissipative and may be included in $b_1(\cdot,\cdot)$ and $b_2(\cdot,\cdot)$ without violating the relaxed coercivity conditions on these forms.

Consider the special case of $r=0$ ($\Longleftrightarrow c=0$). This stability analysis still holds. The quantity g becomes the time integral of fluid–structure velocity difference and may be construed as a fluid–structure displacement. Then the multiplier field acts like a Hookean spring, storing energy $\frac{1}{2}kg^2$ per unit area. This makes clear why it is undesirable to have large oscillations develop in λ, even if steady-state fluid and structure solutions typically remain accurate. A change in boundary conditions could cause energy that has slowly accumulated in λ to be suddenly released back into the fluid and structure subproblems.

Based on this analyis, one might consider altering the formulation for large displacements to integrate the penalty term in the reference configuration, so that the "energy" stored by the multipliers cannot be magnified arbitrarily by in-plane stretching of Γ_t. However, this is unlikely to lead to significant energy build-ups outside of highly contrived cases and we prefer to ensure that the strength of boundary condition enforcement is independent of how stretched or compressed the structure is: the behavior of the fluid problem should be independent of the structure's reference configuration. Further, it may be beneficial to scale the penalty parameter inversely with local measures of background mesh size, when the background mesh is highly nonuniform. While such a scaling would be energetically inconsistent, it may help to reduce the growth of oscillating modes of the multiplier field.

4 Numerical example: a 2D valve

In this section, we look at the performance of our stabilized semi-implicit time integration technique by applying it to a 2D valve, subjected to various boundary conditions. Kamensky et al. [27] investigated the accuracy of the unstabilized semi-implicit scheme with $r=0$ using a similar FSI problem, based on a benchmark proposed by Hesch et al. [105] and later studied by Gil et al. [106] and Wick [52]. The present study is principally concerned with stability rather than accuracy; we refer the reader to our earlier study [27] to see the qualitative convergence of the fluid and structure solutions to a body-fitted reference computation under spatial and temporal refinement.

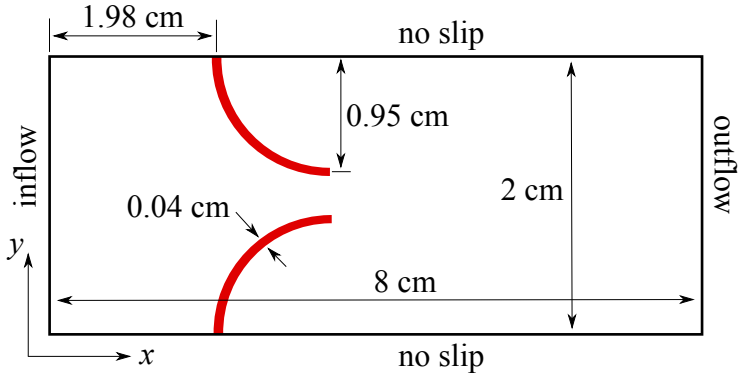

Figure 2: The geometry of the 2D valve problem. (Not to scale.)

4.1 Problem description

The 2D valve model that we study consists of two cantilevered quarter-circular beams attached to the walls of a 2 cm wide and 8 cm long channel filled with incompressible fluid. Figure 2 provides the complete geometry of the problem. The beams are governed by the Kirchhoff–Love shell theory for isotropic St. Venant–Kirchhoff materials described in Section 2.2, which reduces to a beam theory when deformations are constrained to two space dimensions.[‡] The fluid has density $\rho_1 = 1$ g/mL and viscosity $\mu = 3$ cP. These properties mimic those of human blood [107, 108]. We choose the thickness of the beams to be similar to that of an aortic valve leaflet, $h_{\text{th}} = 0.04$ cm [37], and use a Poisson ratio of $\nu = 0.4$ to approximate incompressibility. Values of the Young's modulus vary between computations and are specified in later sections. The top and bottom of the fluid domain have no-slip and no-penetration boundary conditions. The left side of the fluid domain is nominally the inflow and the right side is nominally the outflow. These distinctions are based on the flow direction in which the valve is biased, but, when the nominal inflow and outflow faces are subjected to Neumann boundary conditions, it is possible that fluid may flow into or out of either of these sections of the boundary.

4.2 Steady flow

We first consider the case of a prescribed parabolic flow profile at the inflow boundary. This profile is given by

$$\mathbf{u}_1|_{\text{inflow}} = \left(15 \left\{ \begin{array}{lcl} 0 & , & t < 0 \\ t/(1\text{ s}) & , & 0 \le t < 0.1\text{ s} \\ 0.1 & , & \text{otherwise} \end{array} \right\} \left(\frac{y}{1\text{ cm}}\right)\left(2 - \left(\frac{y}{1\text{ cm}}\right)\right) \text{ cm/s} \right) \mathbf{e}_1 \,. \tag{4.1}$$

[‡]The effective "beam" stiffness of a bending plate is $E/(1-\nu^2)$ rather than E as in the classic Euler–Bernoulli theory.

This profile is represented exactly using the quadratic B-spline shape functions. Taking the characteristic length scale to be the width of the channel and the characteristic velocity to be the peak of the inflow profile at $y = 1$ cm and $t > 0.1$ s, the Reynolds number for this flow is 100. We deliberately select it to be much slower than ejection through a heart valve, to ensure that the fluid–structure system approaches a steady solution as $t \to \infty$, rather than developing a periodic or turbulent solution. We assign the beams composing the valve a Young's modulus of $E = 10^5$ dyn/cm^2. This value is selected to ensure significant structural deformation in this flow regime.

To study the effect of the stabilization parameter, r, and the mesh size, h, on this problem, we introduce a hierarchy of three fluid meshes, M1, M2, and M3, consisting of 32×128 (h=0.0625 cm), 64×256 (h=0.03125 cm), and 128×512 (h=0.015625 cm) quadratic B-spline elements, respectively. We employ a single discretization of the beams, which divides each of the quarter-circular arcs into 64 quadratic NURBS elements. The NURBS elements are capable of exactly representing the circular geometry at any resolution [53]. As suggested by Eq. (2.12), we assign the penalties τ^B_{NOR} and τ^B_{TAN} according to the formula

$$\tau^B_{\mathrm{NOR}} = \tau^B_{\mathrm{TAN}} = C\mu/h \,, \tag{4.2}$$

with $C = 10^2$. To ensure that the time step has a fixed proportionality to the element advective time scale (see Bazilevs et al. [91, page 181]), we assign time step sizes using the formula

$$\Delta t = \frac{h}{6.25 \text{ cm/s}} \,. \tag{4.3}$$

We compute solutions for M1–M3 using the semi-implicit time integration scheme described in Section 3, with $r = 1$, $r = 0.1$, and $r = 0$ (no stabilization).

The $L^2(\Gamma_t)$-norm of λ is shown as a function of time for each case in Figure 3. We can see that both refinement and increased r reduce the norm at which λ reaches a steady value. While it might seem that multiplier fields differing greatly in L^2 norm would produce wildly different fluid velocity fields and/or structure deformation solutions, this is not the case. Figure 4 compares the structure deformation and velocity fields for $r = 1$, $r = 0.1$, and $r = 0$ at time $t = 10$ s on M1–M3. The corresponding Lagrange multiplier force fields on the structure are plotted in Figure 5. We see that the difference in L^2 norm between the multiplier fields is due to oscillatory modes that have very little influence on the steady-state fluid and structure solutions. As pointed out in Section 3.2, though, these modes carry potential energy, and should not be allowed to grow *ad infinitum*, as they appear to in the case of $r = 0$. This growth is not contradictory to the energy analysis of Section 3.2. The inhomogeneous essential boundary condition on the inflow face does work on the system, feeding it energy that was not present in the initial condition. Evidently, this energy can accumulate in the multiplier field. While the accumulation of excess stored energy in the multiplier field has clear disadvantages, selecting r large enough to completely eliminate oscillations may result in unacceptable leakage through structures, as demonstrated in the following section. For a fixed value of r, both leakage and oscillation may be reduced through refinement, but, in practice, we recommend

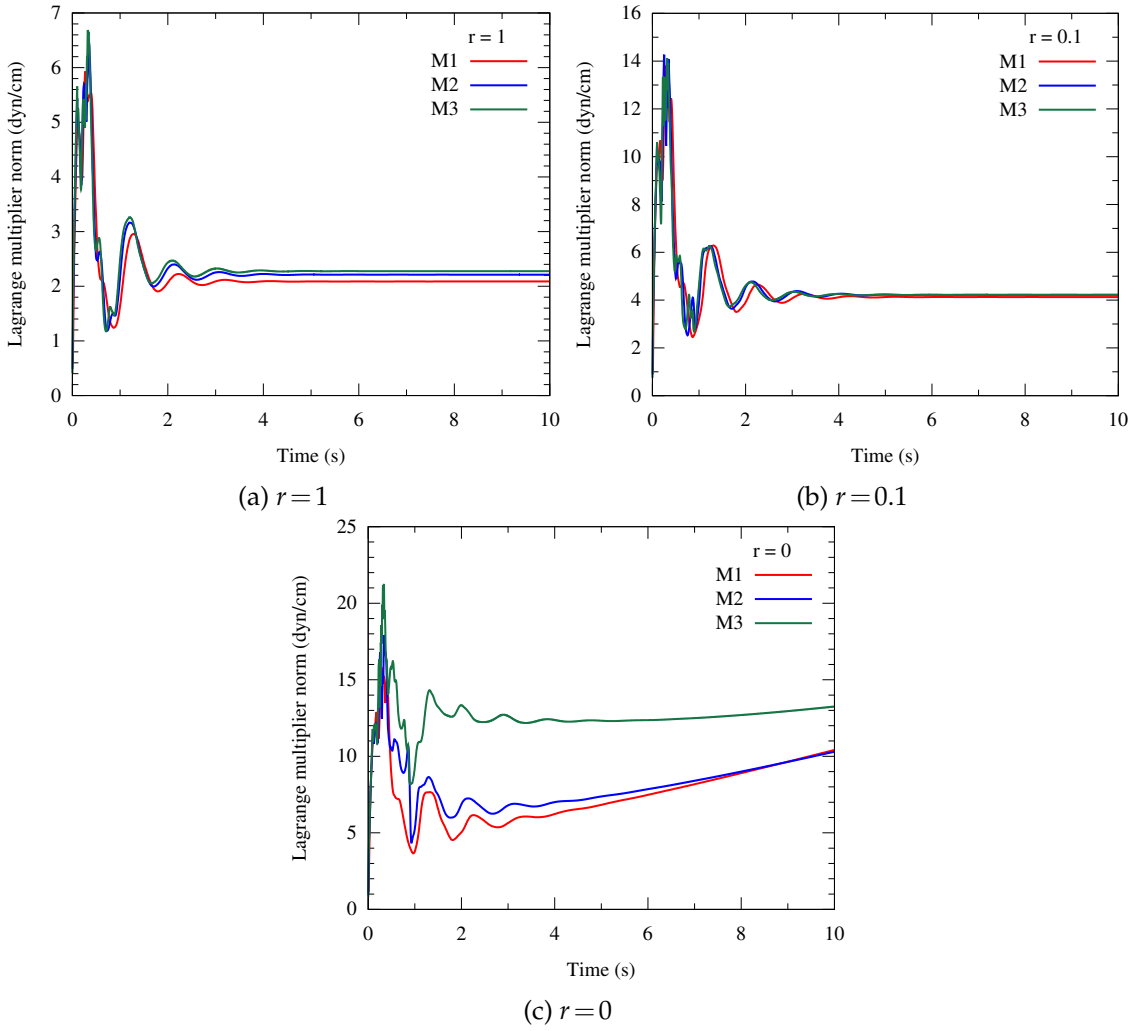

(a) $r=1$ (b) $r=0.1$

(c) $r=0$

Figure 3: The L^2 norms of the Lagrange multiplier field as functions of time for steady flow through the 2D valve, with (a) $r=1$; (b) $r=0.1$. Note the difference in scale from (a); (c) $r=0$, i.e. no stabilization. Note that they do not reach steady values in this case.

tuning r to obtain the best quality solution within the constraints of available time and computational resources.

The fact that $\|\lambda\|_{L^2}$ during the transient stage of the computations with $r=0$ increases with refinement does not indicate that refinement harms the stability of the semi-implicit scheme. In fact, as we approach the exact solution, we cannot expect the $L^2(\Gamma_t)$ norm of the pressure jump to converge; for viscous incompressible flow around the edge of a thin plate, the pressure distribution on the plate is not necessarily square-integrable. A famous example is Hasimoto's solution of Stokes flow through an aperture [109, Eq. (4.8)].

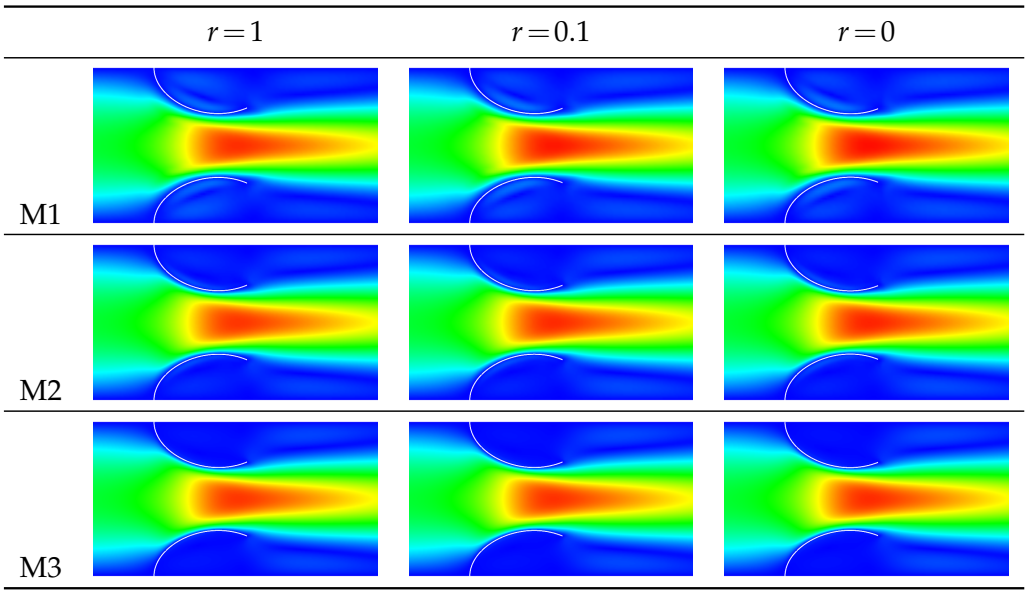

Figure 4: Comparisons of structure deformation and fluid velocity magnitude fields at time $t = 10$ s, computed on M3, with different stabilization parameters. Color scale: 0 (blue) to 3.4 cm/s (red).

The energy analysis of Section 3.2 suggests that the L^2 norm of λ is a natural choice for investigating semi-discrete stability, but it should not be used in assessing convergence with spatial refinement. We can see from Figure 3(c) the rate of growth of oscillations in the steady state decreases with refinement, indicating greater stability on finer meshes.

4.3 Convergence to a hydrostatic solution during closure

We now consider the case of the 2D valve's closure when subjected to Neumann boundary conditions. Because a 2D model cannot accurately represent the mechanics of a 3D shell structure, we must make the beams significantly stiffer than the soft tissues appearing in native or bioprosthetic heart valves, to prevent the 2D valve from prolapsing when subjected to realistic pressure differences. We therefore use a Young's modulus of $E = 7 \times 10^9$ dyn/cm^2 in this example. Contact between the leaflets is an essential aspect of valve closure. For the computations in this section, we use parameters $k_c = 10^8$ dyn/cm^3, $c_c = 0.1$ cm, and $h_c = 0.01$ cm in the penalty method described in Section 2.2. At the inflow, we apply a zero-traction boundary condition and, at the outflow, we apply the following time-dependent pressure:

$$P_{\text{out}}(t) = \left\{ \begin{array}{lll} 0 & , & t \leq 0 \\ 1000\left(\frac{t}{1\,\text{s}}\right) & , & 0 < t < 0.1\ \text{s} \\ 100 & , & \text{otherwise} \end{array} \right\} \text{mmHg}. \tag{4.4}$$

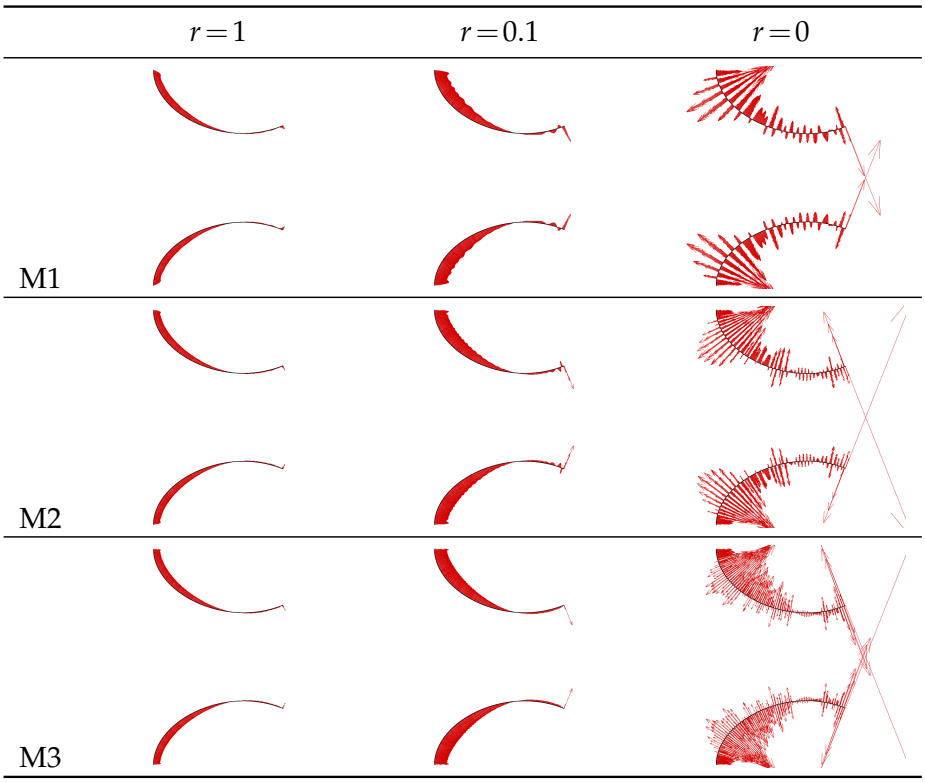

Figure 5: The forces on the structure due to the Lagrange multiplier field in the solutions from Figure 4.

This approximates the pressure difference across a closed heart valve in the physiological setting [110]. Recall from the blocked plug flow model Section 3.1 that, as the system approaches a steady solution, we expect some leakage for $r > 0$ that, as $r \to 0$, will be proportional to r and inversely proportional to τ^B_{NOR}. This is complicated somewhat in practice, because constraint violation is not the only source of apparent leakage: as demonstrated by Kamensky et al. [27, Section 4.4], approximation error in the pressure can lead to violation of the continuity equation, which leads, in turn, to "leakage" through the valve, even when the fluid and structure velocities match. For the computations in this section, we set $s^{\text{shell}} = 10^8$ to diminish this source of leakage such that it is small enough to clearly distinguish the effect of r.

We employ the fluid mesh M1 and structure meshes defined in the previous section. We reduce the time step by a factor of 10 to improve nonlinear convergence and increase penalties by a factor of 1000 to more strongly enforce the no-penetration condition. For the computations of this section,

$$\Delta t = \frac{h}{62.5 \text{ cm/s}} \qquad \text{and} \qquad \tau^B_{\text{NOR}} = \tau^B_{\text{TAN}} = C\mu/h \,, \tag{4.5}$$

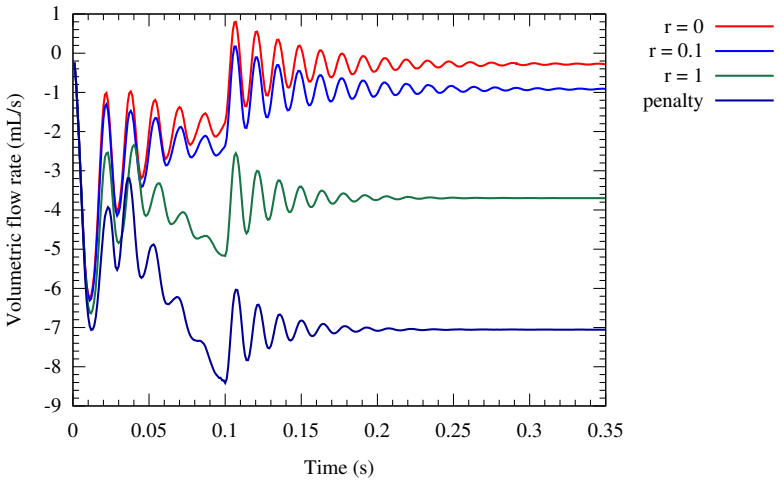

Figure 6: Volumetric flow rate through the closing valve as a function of time, for different values of r.

with $C = 10^5$. We compute solutions with $r = \infty$ (velocity penalization), $r = 1$, $r = 0.1$, and $r = 0$. Figure 6 shows the volumetric flow through the outflow face as a function of time for each value of r. Approximate asymptotic values of the steady-state flow rate are given in Table 1, along with the crude estimates based on Eq. (3.21) from the plug flow model of Section 3.1. The plug flow model consistently underestimates leakage, due to the imperfect local mass conservation mentioned above. The L^2 norms of λ for each finite value of r are given as functions of time in Figure 7. For $r = 0$, the asymptotic value[§] of $\|\lambda\|_{L^2}$ approximately matches the rough estimate of $\sqrt{A(\Delta P)^2}$ for A equal to the surface area of the beams and $\Delta P = 100$ mmHg. Figure 8 compares the solutions at time $t = 0.35$ s for $r = 1$ and $r = 0$. We can see that the structure deformations and fluid pressure fields are nearly indistinguishable, but the solution with $r = 1$ has a more stable multiplier field at the expense of spurious flow in what should be a hydrostatic solution.

Remark 4.1. The increase of C to 10^5 in the definition of $\tau^B_{(\cdot)}$ for the closed valve computations is largely for the benefit of computations with $r > 0$. While exploring the parameter space, we found that wide ranges of C produced reasonable results with $r = 0$ (and, we presume, would be effective with $r \ll 1$), but smaller values of C led to large flow rates for $r \geq 0.1$. Significant inflow through Neumann boundary conditions is unstable and prone to "backflow divergence". This instability can be avoided in practical computations by including backflow stabilization [111], as reviewed by Esmaily-Moghadam et al. [112] and applied in our 3D valve simulations [26, 27], but we have not included any such stabilization in the present work, to avoid complicating the analogy to the plug flow model

[§]If the simulation is continued for a much longer period, it becomes clear that $\|\lambda\|^2_{L^2}$ grows, but at a much slower rate (relative to $|\lambda|$) than in the case of the open valve; on the time scale of ~ 0.5 s, it effectively flatlines.

r	computed leakage (mL/s)	plug flow estimate (mL/s)
∞	-7.1	-5.6
1	-3.7	-2.8
0.1	-0.9	-0.5
0	-0.3	0

Table 1: Steady volumetric flux (assuming 1 cm depth) through the closed 2D valve for different values of r, alongside the values estimated from the plug flow model of Section 3.1, which neglects leakage due to spurious volume loss.

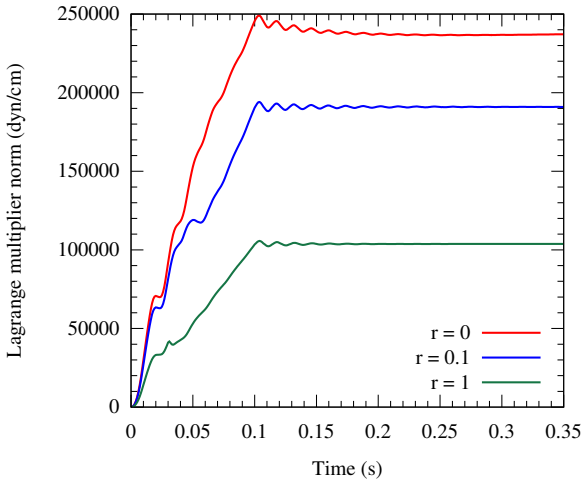

Figure 7: $L^2(\Gamma_t)$ norm of λ on closing valve as a function of time, for finite values of r. (For $r=\infty$, it will be zero $\forall t$.)

of Section 3.1.

Remark 4.2. The skeptical reader may suspect that the oscillation in volumetric flow rate is a spurious phenomenon, due to the damped spring interpretation of the multiplier forcing. However, the characteristic frequency of the fluid mass attached to the multiplier "spring" is much higher and the oscillation's presence in the penalty solution with $r=\infty$ rules out this hypothesis altogether. The oscillation is the reverberation of the water hammer on the closed elastic valve. We observed a similar effect in our simulations of a 3D valve and provided an electronic–hydraulic analogy [113] to the familiar transient response of a series RLC circuit [27, Figure 29].

Remark 4.3. Notice in Figure 8 that, for $r=1$, large vortices form on the concave sides of the leaflets. These are features of the steady solution (which should be hydrostatic). A closer examination of the flow field shows that the upper vortex is counterclockwise and the lower is clockwise. These vortices are fed by flow between themselves and the walls, which is permitted by leakage through the portions of the leaflets closer to the walls. The

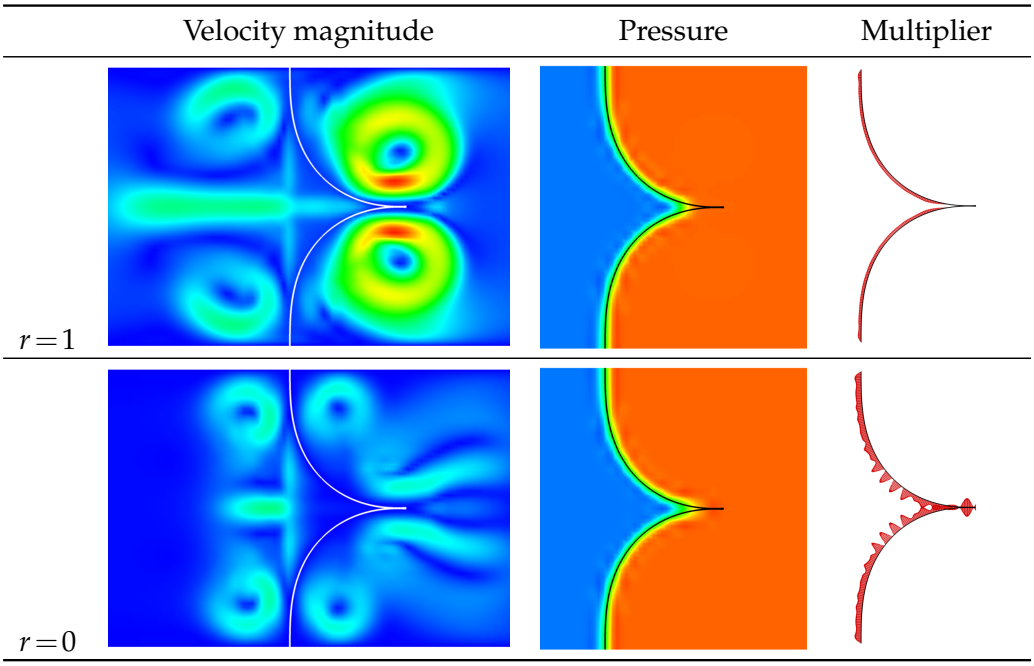

Figure 8: Velocity, pressure, and multiplier solutions at $t = 0.35$ s for the closed valve with $r = 1$ and $r = 0$. See Remark 4.3 for discussion on the velocity fields. Velocity color scale: 0 (blue) to 24 cm/s (red). Pressure color scale: -20000 dyn/cm^2 (blue) to 150000 dyn/cm^2 (red).

velocity magnitude in the vortices is significantly larger than that of the flow through the leaflets, which underscores the importance of preventing unphysical leakage to obtaining reasonable solutions.

5 Conclusion

We find that, on problems with non-hydrostatic steady solutions, the semi-implicit time integration scheme proposed for unsteady fluid–thin structure interaction by Kamensky et al. [27] (and reiterated in Section 3 of this paper) may lead to oscillatory Lagrange multiplier fields that grow in L^2 norm over time. Section 3 introduces a family of stabilized time integration schemes parameterized by $r \in [0,\infty]$, which represents a trade-off between stability and strength of constraint enforcement. For $r = 0$, we recover the original semi-implicit integration scheme, which can enforce constraints very strongly, but leads to oscillatory multiplier fields that, in some computations, may grow over time. For $r = \infty$, we obtain a penalty method in which the Lagrange multiplier field is zero, but some problems require impractically large penalty values to obtain satisfactory constraint enforcement. For intermediate values, one may use the rules of thumb given in

Section 3.1 to anticipate the strength of constraint enforcement and potential growth of the Lagrange multiplier field.

In practice, oscillatory multiplier fields lead to reasonable fluid and structure solutions, as evidenced by Figures 4 and 5, and by our earlier simulations using $r=0$ [26,27]. Based on the findings of this study, we recommend to favor constraint enforcement over stable multiplier approximation by choosing r significantly smaller than one. This will capture the critical solution features of the fluid and structure subproblems on coarser meshes, but still prevents the Lagrange multipliers from growing to infinity in the long-time limit, as they may with $r=0$, even in the extreme case of a structure held rigidly against a contradictory fluid Dirichlet boundary condition (Section 3.1.3). We also observed, as noted in Remark 4.1, that smaller values of r reduce the sensitivity of the fluid and structure solutions to the choice of penalty parameter. For $r \ll 1$, we suggest to view the multiplier field as an intermediate by-product of the constraint enforcement rather than a solution variable, since its point values may be grossly in error. If point values of the pressure jump across a thin structure are needed, it may be possible to post-process the oscillatory multiplier field with smoothing procedures, similar to those applied to oscillatory pressures resulting from penalty formulations of incompressible solid and fluid mechanics [114]. We might also consider inserting such a spatial smoothing step into the semi-implicit integration loop.

Acknowledgments

D. Kamensky was partially supported by the CSEM Graduate Fellowship. J.A. Evans was partially supported by the ICES Postdoctoral Fellowship at the Institute for Computational Engineering and Sciences. M.-C. Hsu was partially supported by ARO grant No. W911NF-14-1-0296. We thank the Texas Advanced Computing Center (TACC) at the University of Texas at Austin for providing HPC resources that have contributed to the research results reported in this paper. Lastly, we congratulate Tony Wen-Hann Sheu on his 60$^{\text{th}}$ birthday, and wish him continued productivity in his research and teaching.

References

[1] K. Stein, R. Benney, V. Kalro, T. E. Tezduyar, J. Leonard, and M. Accorsi. Parachute fluid–structure interactions: 3-D Computation. *Computer Methods in Applied Mechanics and Engineering*, 190:373–386, 2000.

[2] T. Tezduyar and Y. Osawa. Fluid–structure interactions of a parachute crossing the far wake of an aircraft. *Computer Methods in Applied Mechanics and Engineering*, 191:717–726, 2001.

[3] K. Stein, T. E. Tezduyar, S. Sathe, R. Benney, and R. Charles. Fluid-structure interaction modeling of parachute soft-landing dynamics. *International Journal for Numerical Methods in Fluids*, 47:619–631, 2005.

[4] T. E. Tezduyar, S. Sathe, J. Pausewang, M. Schwaab, J. Christopher, and J. Crabtree. Fluid–structure interaction modeling of ringsail parachutes. *Computational Mechanics*, 43:133–142, 2008.

[5] K. Takizawa, S. Wright, C. Moorman, and T. E. Tezduyar. Fluid–structure interaction modeling of parachute clusters. *International Journal for Numerical Methods in Fluids*, 65:286–307, 2011.

[6] K. Takizawa, T. Spielman, and T. E. Tezduyar. Space–time FSI modeling and dynamical analysis of spacecraft parachutes and parachute clusters. *Computational Mechanics*, 48:345–364, 2011.

[7] K. Takizawa and T. E. Tezduyar. Computational methods for parachute fluid–structure interactions. *Archives of Computational Methods in Engineering*, 19:125–169, 2012.

[8] K. Takizawa, T. E. Tezduyar, R. Kolesar C. Boswell, and K. Montel. FSI modeling of the reefed stages and disreefing of the Orion spacecraft parachutes. *Computational Mechanics*, 54:1203–1220, 2014.

[9] K. Takizawa, B. Henicke, A. Puntel, N. Kostov, and T. E. Tezduyar. Space–time techniques for computational aerodynamics modeling of flapping wings of an actual locust. *Computational Mechanics*, 50:743–760, 2012.

[10] K. Takizawa, B. Henicke, A. Puntel, N. Kostov, and T. E. Tezduyar. Computer modeling techniques for flapping-wing aerodynamics of a locust. *Computers & Fluids*, 85:125–134, 2013.

[11] K. Takizawa, T. E. Tezduyar, and N. Kostov. Sequentially-coupled space–time FSI analysis of bio-inspired flapping-wing aerodynamics of an MAV. *Computational Mechanics*, 54:213–233, 2014.

[12] V. B. Makhijani, H. Q. Yang, P. J. Dionne, and M. J. Thubrikar. Three-dimensional coupled fluid–structure simulation of pericardial bioprosthetic aortic valve function. *ASAIO Journal*, 43:M387–M392, 1997.

[13] J. De Hart, G. W. M. Peters, P. J. G. Schreurs, and F. P. T. Baaijens. A three-dimensional computational analysis of fluid–structure interaction in the aortic valve. *Journal of Biomechanics*, 36:103–112, 2003.

[14] J. De Hart, F. P. T. Baaijens, G. W. M. Peters, and P. J. G. Schreurs. A computational fluid–structure interaction analysis of a fiber-reinforced stentless aortic valve. *Journal of Biomechanics*, 36:699–712, 2003.

[15] R. Cheng, Y. G. Lai, and K. B. Chandran. Three-dimensional fluid-structure interaction simulation of bileaflet mechanical heart valve flow dynamics. *Annals of Biomedical Engineering*, 32(11):1471–1483, 2004.

[16] C. J. Carmody, G. Burriesci, I. C. Howard, and E. A. Patterson. An approach to the simulation of fluid–structure interaction in the aortic valve. *Journal of Biomechanics*, 39:158–169, 2006.

[17] R. van Loon, P. D. Anderson, and F. N. van de Vosse. A fluid–structure interaction method with solid-rigid contact for heart valve dynamics. *Journal of Computational Physics*, 217:806–823, 2006.

[18] M. Astorino, J.-F. Gerbeau, O. Pantz, and K.-F. Traoré. Fluid–structure interaction and multi-body contact: Application to aortic valves. *Computer Methods in Applied Mechanics and Engineering*, 198:3603–3612, 2009.

[19] I. Borazjani, L. Ge, and F. Sotiropoulos. High-resolution fluid–structure interaction simulations of flow through a bi-leaflet mechanical heart valve in an anatomic aorta. *Annals of Biomedical Engineering*, 38(2):326–344, 2010.

[20] R. van Loon. Towards computational modelling of aortic stenosis. *International Journal for Numerical Methods in Biomedical Engineering*, 26:405–420, 2010.
[21] S. C. Shadden, M. Astorino, and J.-F. Gerbeau. Computational analysis of an aortic valve jet with Lagrangian coherent structures. *Chaos*, 20:017512, 2010.
[22] B. E. Griffith. Immersed boundary model of aortic heart valve dynamics with physiological driving and loading conditions. *International Journal for Numerical Methods in Biomedical Engineering*, 28(3):317–345, 2012.
[23] F. Sturla, E. Votta, M. Stevanella, C. A. Conti, and A. Redaelli. Impact of modeling fluid–structure interaction in the computational analysis of aortic root biomechanics. *Medical Engineering and Physics*, 35:1721–1730, 2013.
[24] I. Borazjani. Fluid–structure interaction, immersed boundary-finite element method simulations of bio-prosthetic heart valves. *Computer Methods in Applied Mechanics and Engineering*, 257:103–116, 2013.
[25] E. Votta, T. B. Le, M. Stevanella, L. Fusini, E. G. Caiani, A. Redaelli, and F. Sotiropoulos. Toward patient-specific simulations of cardiac valves State-of-the-art and future directions. *Journal of Biomechanics*, 46:217–228, 2013.
[26] M.-C. Hsu, D. Kamensky, Y. Bazilevs, M. S. Sacks, and T. J. R. Hughes. Fluid–structure interaction analysis of bioprosthetic heart valves: significance of arterial wall deformation. *Computational Mechanics*, 54:1055–1071, 2014.
[27] D. Kamensky, M.-C. Hsu, D. Schillinger, J. A. Evans, A. Aggarwal, Y. Bazilevs, M. S. Sacks, and T. J. R. Hughes. An immersogeometric variational framework for fluid–structure interaction: Application to bioprosthetic heart valves. *Computer Methods in Applied Mechanics and Engineering*, 284:1005–1053, 2015.
[28] F. J. Schoen and R. J. Levy. Calcification of tissue heart valve substitutes: progress toward understanding and prevention. *Ann. Thorac. Surg.*, 79(3):1072–1080, 2005.
[29] P. Pibarot and J. G. Dumesnil. Prosthetic heart valves: selection of the optimal prosthesis and long-term management. *Circulation*, 119(7):1034–1048, 2009.
[30] R. F. Siddiqui, J. R. Abraham, and J. Butany. Bioprosthetic heart valves: modes of failure. *Histopathology*, 55:135–144, 2009.
[31] M. S. Hamid, H. N. Sabbah, and P. D. Stein. Finite element evaluation of stresses on closed leaflets of bioprosthetic heart valves with flexible stents. *Finite Elements in Analysis and Design*, 1(3):213–225, 1985.
[32] M. S. Hamid, H. N. Sabbah, and P. D. Stein. Influence of stent height upon stresses on the cusps of closed bioprosthetic valves. *Journal of Biomechanics*, 19(9):759–769, 1986.
[33] E. P. Rousseau, A. A. van Steenhoven, and J. D. Janssen. A mechanical analysis of the closed Hancock heart valve prosthesis. *Journal of Biomechanics*, 21(7):545–562, 1988.
[34] K. B. Chandran, S. H. Kim, and G. Han. Stress distribution on the cusps of a polyurethane trileaflet heart valve prosthesis in the closed position. *Journal of Biomechanics*, 24(6):385–395, 1991.
[35] M. M. Black, I. C. Howard, X. Huang, and E. A. Patterson. A three-dimensional analysis of a bioprosthetic heart valve. *Journal of Biomechanics*, 24(9):793–801, 1991.
[36] E. A. Patterson, I. C. Howard, and M. A. Thornton. A comparative study of linear and nonlinear simulations of the leaflets in a bioprosthetic heart valve during the cardiac cycle. *J Med Eng Technol*, 20(3):95–108, 1996.
[37] J. Li, X. Y. Luo, and Z. B. Kuang. A nonlinear anisotropic model for porcine aortic heart valves. *Journal of Biomechanics*, 34(10):1279–1289, 2001.
[38] V. C. Sripathi, R. K. Kumar, and K. R. Balakrishnan. Further insights into normal aortic

valve function: role of a compliant aortic root on leaflet opening and valve orifice area. *Ann. Thorac. Surg.*, 77(3):844–851, 2004.

[39] W. Sun, A. Abad, and M. S. Sacks. Simulated bioprosthetic heart valve deformation under quasi-static loading. *Journal of Biomechanical Engineering*, 127(6):905–914, 2005.

[40] H. Kim, J. Lu, M. S. Sacks, and K. B. Chandran. Dynamic simulation pericardial bioprosthetic heart valve function. *Journal of Biomechanical Engineering*, 128:717–724, 2006.

[41] H. Kim, J. Lu, M. S. Sacks, and K. B. Chandran. Dynamic simulation of bioprosthetic heart valves using a stress resultant shell model. *Annals of Biomedical Engineering*, 36(2):262–275, 2008.

[42] F. Auricchio, M. Conti, S. Morganti, and P. Totaro. A computational tool to support pre-operative planning of stentless aortic valve implant. *Medical Engineering and Physics*, 33(10):1183–1192, 2011.

[43] P. E. Hammer, M. S. Sacks, P. J. Del Nido, and R. D. Howe. Mass-spring model for simulation of heart valve tissue mechanical behavior. *Annals of Biomedical Engineering*, 39(6):1668–1679, 2011.

[44] F. Auricchio, M. Conti, S. Morganti, and A. Reali. Simulation of transcatheter aortic valve implantation: a patient-specific finite element approach. *Computer Methods in Biomechanics and Biomedical Engineering*, 17(12):1347–1357, 2013.

[45] R. Fan, A. S. Bayoumi, P. Chen, C. M. Hobson, W. R. Wagner, J. E. Mayer Jr., and M. S. Sacks. Optimal elastomeric scaffold leaflet shape for pulmonary heart valve leaflet replacement. *Journal of Biomechanics*, 46:662–669, 2013.

[46] F. Auricchio, M. Conti, A. Ferrara, S. Morganti, and A. Reali. Patient-specific simulation of a stentless aortic valve implant: the impact of fibres on leaflet performance. *Computer Methods in Biomechanics and Biomedical Engineering*, 17(3):277–285, 2014.

[47] S. Morganti, F. Auricchio, D. J. Benson, F. I. Gambarin, S. Hartmann, T. J. R. Hughes, and A. Reali. Patient-specific isogeometric structural analysis of aortic valve closure. *Computer Methods in Applied Mechanics and Engineering*, 284:508–520, 2015.

[48] T. J. R. Hughes, W. K. Liu, and T. K. Zimmermann. Lagrangian–Eulerian finite element formulation for incompressible viscous flows. *Computer Methods in Applied Mechanics and Engineering*, 29:329–349, 1981.

[49] J. Donea, S. Giuliani, and J. P. Halleux. An arbitrary Lagrangian–Eulerian finite element method for transient dynamic fluid–structure interactions. *Computer Methods in Applied Mechanics and Engineering*, 33:689–723, 1982.

[50] J. Donea, A. Huerta, J.-P. Ponthot, and A. Rodriguez-Ferran. Arbitrary Lagrangian–Eulerian methods. In *Encyclopedia of Computational Mechanics*, Volume 3: Fluids, chapter 14. John Wiley & Sons, 2004.

[51] T. E. Tezduyar, K. Takizawa, C. Moorman, S. Wright, and J. Christopher. Space–time finite element computation of complex fluid–structure interactions. *International Journal for Numerical Methods in Fluids*, 64:1201–1218, 2010.

[52] T. Wick. Flapping and contact FSI computations with the fluid–solid interface-tracking/interface-capturing technique and mesh adaptivity. *Computational Mechanics*, 53(1):29–43, 2014.

[53] L. Piegl and W. Tiller. *The NURBS Book (Monographs in Visual Communication), 2nd ed.* Springer-Verlag, New York, 1997.

[54] T. J. R. Hughes, J. A. Cottrell, and Y. Bazilevs. Isogeometric analysis: CAD, finite elements, NURBS, exact geometry, and mesh refinement. *Computer Methods in Applied Mechanics and Engineering*, 194:4135–4195, 2005.

[55] D. Schillinger, L. Dedè, M. A. Scott, J. A. Evans, M. J. Borden, E. Rank, and T. J. R. Hughes. An isogeometric design-through-analysis methodology based on adaptive hierarchical refinement of NURBS, immersed boundary methods, and T-spline CAD surfaces. *Computer Methods in Applied Mechanics and Engineering*, 249–252:116–150, 2012.

[56] M. Breitenberger, A. Apostolatos, B. Philipp, R. Wüchner, and K.-U. Bletzinger. Analysis in computer aided design: Nonlinear isogeometric B-Rep analysis of shell structures. *Computer Methods in Applied Mechanics and Engineering*, 284:401–457, 2015.

[57] J. A. Cottrell, A. Reali, Y. Bazilevs, and T. J. R. Hughes. Isogeometric analysis of structural vibrations. *Computer Methods in Applied Mechanics and Engineering*, 195:5257–5297, 2006.

[58] J. A. Cottrell, T. J. R. Hughes, and A. Reali. Studies of refinement and continuity in isogeometric structural analysis. *Computer Methods in Applied Mechanics and Engineering*, 196:4160–4183, 2007.

[59] J. A. Cottrell, T. J. R. Hughes, and Y. Bazilevs. *Isogeometric Analysis: Toward Integration of CAD and FEA*. Wiley, Chichester, 2009.

[60] D. J. Benson, Y. Bazilevs, M.-C. Hsu, and T. J. R. Hughes. Isogeometric shell analysis: The Reissner–Mindlin shell. *Computer Methods in Applied Mechanics and Engineering*, 199:276–289, 2010.

[61] Y. Bazilevs and T. J. R. Hughes. NURBS-based isogeometric analysis for the computation of flows about rotating components. *Computational Mechanics*, 43:143–150, 2008.

[62] Y. Bazilevs and I. Akkerman. Large eddy simulation of turbulent Taylor–Couette flow using isogeometric analysis and the residual–based variational multiscale method. *Journal of Computational Physics*, 229:3402–3414, 2010.

[63] J. A. Evans and T. J. R. Hughes. Isogeometric divergence-conforming B-splines for the unsteady Navier–Stokes equations. *Journal of Computational Physics*, 241:141–167, 2013.

[64] L. De Lorenzis, İ. Temizer, P. Wriggers, and G. Zavarise. A large deformation frictional contact formulation using NURBS-based isogeometric analysis. *International Journal for Numerical Methods in Engineering*, 87:1278–1300, 2011.

[65] İ. Temizer, P. Wriggers, and T. J. R. Hughes. Three-dimensional mortar-based frictional contact treatment in isogeometric analysis with NURBS. *Computer Methods in Applied Mechanics and Engineering*, 209-212:115–128, 2012.

[66] L. De Lorenzis, P. Wriggers, and T. J. R. Hughes. Isogeometric contact: a review. *GAMM-Mitteilungen*, 37(1):85–123, 2014.

[67] J. Kiendl, K.-U. Bletzinger, J. Linhard, and R. Wüchner. Isogeometric shell analysis with Kirchhoff–Love elements. *Computer Methods in Applied Mechanics and Engineering*, 198:3902–3914, 2009.

[68] J. Kiendl, Y. Bazilevs, M.-C. Hsu, R. Wüchner, and K.-U. Bletzinger. The bending strip method for isogeometric analysis of Kirchhoff–Love shell structures comprised of multiple patches. *Computer Methods in Applied Mechanics and Engineering*, 199:2403–2416, 2010.

[69] J. Kiendl. *Isogeometric Analysis and Shape Optimal Design of Shell Structures*. PhD thesis, Lehrstuhl für Statik, Technische Universität München, 2011.

[70] D. J. Benson, Y. Bazilevs, M.-C. Hsu, and T. J. R. Hughes. A large deformation, rotation-free, isogeometric shell. *Computer Methods in Applied Mechanics and Engineering*, 200:1367–1378, 2011.

[71] E. Rank, M. Ruess, S. Kollmannsberger, D. Schillinger, and A. Düster. Geometric modeling, isogeometric analysis and the finite cell method. *Computer Methods in Applied Mechanics and Engineering*, 249-252:104–115, 2012.

[72] M. Ruess, D. Schillinger, Y. Bazilevs, V. Varduhn, and E. Rank. Weakly enforced essential

boundary conditions for NURBS-embedded and trimmed NURBS geometries on the basis of the finite cell method. *International Journal for Numerical Methods in Engineering*, 95:811–846, 2013.

[73] D. Schillinger and M. Ruess. The Finite Cell Method: A review in the context of higher-order structural analysis of CAD and image-based geometric models. *Archives of Computational Methods in Engineering*, 22(3):391–455, 2015.

[74] H. J. C. Barbosa and T. J. R. Hughes. The finite element method with Lagrange multipliers on the boundary: circumventing the Babuška-Brezzi condition. *Computer Methods in Applied Mechanics and Engineering*, 85(1):109–128, 1991.

[75] Y. Bazilevs, M.-C. Hsu, and M. A. Scott. Isogeometric fluid–structure interaction analysis with emphasis on non-matching discretizations, and with application to wind turbines. *Computer Methods in Applied Mechanics and Engineering*, 249–252:28–41, 2012.

[76] J. Nitsche. Über ein Variationsprinzip zur Lösung von Dirichlet-Problemen bei Verwendung von Teilräumen, die keinen Randbedingungen unterworfen sind. *Abhandlungen aus dem Mathematischen Seminar der Universität Hamburg*, 36:9–15, 1971.

[77] A. Hansbo and P. Hansbo. An unfitted finite element method, based on Nitsche's method, for elliptic interface problems. *Computer Methods in Applied Mechanics and Engineering*, 191:5537–5552, 2002.

[78] J. Juntunen and R. Stenberg. Nitsche's method for general boundary conditions. *Mathematics of Computation*, 78:1353–1374, 2009.

[79] A. Embar, J. Dolbow, and I. Harari. Imposing Dirichlet boundary conditions with Nitsche's method and spline-based finite elements. *International Journal for Numerical Methods in Engineering*, 83:877–898, 2010.

[80] Y. Bazilevs and T. J. R. Hughes. Weak imposition of Dirichlet boundary conditions in fluid mechanics. *Computers and Fluids*, 36:12–26, 2007.

[81] Y. Bazilevs, C. Michler, V. M. Calo, and T. J. R. Hughes. Weak Dirichlet boundary conditions for wall-bounded turbulent flows. *Computer Methods in Applied Mechanics and Engineering*, 196:4853–4862, 2007.

[82] Y. Bazilevs, C. Michler, V. M. Calo, and T. J. R. Hughes. Isogeometric variational multiscale modeling of wall-bounded turbulent flows with weakly enforced boundary conditions on unstretched meshes. *Computer Methods in Applied Mechanics and Engineering*, 199:780–790, 2010.

[83] M.-C. Hsu, I. Akkerman, and Y. Bazilevs. Wind turbine aerodynamics using ALE–VMS: Validation and the role of weakly enforced boundary conditions. *Computational Mechanics*, 50:499–511, 2012.

[84] S. C. Brenner and L. R. Scott. *The Mathematical Theory of Finite Element Methods, 3rd ed.* Springer, 2008.

[85] A. Johansson and M. G. Larson. A high order discontinuous Galerkin Nitsche method for elliptic problems with fictitious boundary. *Numerische Mathematik*, 123:607–628, 2012.

[86] J. A. Evans and T. J. R. Hughes. Explicit trace inequalities for isogeometric analysis and parametric hexahedral finite elements. *Numerische Mathematik*, 123:259–290, 2013.

[87] A. N. Brooks and T. J. R. Hughes. Streamline upwind/Petrov-Galerkin formulations for convection dominated flows with particular emphasis on the incompressible Navier-Stokes equations. *Computer Methods in Applied Mechanics and Engineering*, 32:199–259, 1982.

[88] L. P. Franca, S. L. Frey, and T. J. R. Hughes. Stabilized finite element methods: I. Application to the advective-diffusive model. *Computer Methods in Applied Mechanics and Engineering*, 95:253–276, 1992.

[89] F. Hartmann. The discrete Babuška-Brezzi condition. *Ingenieur-Archiv*, 56(3):221–228, 1986.
[90] T. J. R. Hughes, G. R. Feijóo, L. Mazzei, and J. B. Quincy. The variational multiscale method–A paradigm for computational mechanics. *Computer Methods in Applied Mechanics and Engineering*, 166:3–24, 1998.
[91] Y. Bazilevs, V. M. Calo, J. A. Cottrel, T. J. R. Hughes, A. Reali, and G. Scovazzi. Variational multiscale residual-based turbulence modeling for large eddy simulation of incompressible flows. *Computer Methods in Applied Mechanics and Engineering*, 197:173–201, 2007.
[92] C. A. Taylor, T. J. R. Hughes, and C. K. Zarins. Finite element modeling of blood flow in arteries. *Computer Methods in Applied Mechanics and Engineering*, 158:155–196, 1998.
[93] G. A. Holzapfel. *Nonlinear Solid Mechanics: A Continuum Approach for Engineering*. Wiley, Chichester, 2000.
[94] J. Chung and G. M. Hulbert. A time integration algorithm for structural dynamics with improved numerical dissipation: The generalized-α method. *Journal of Applied Mechanics*, 60:371–75, 1993.
[95] Y. Bazilevs, V. M. Calo, T. J. R. Hughes, and Y. Zhang. Isogeometric fluid–structure interaction: theory, algorithms, and computations. *Computational Mechanics*, 43:3–37, 2008.
[96] K. E. Jansen, C. H. Whiting, and G. M. Hulbert. A generalized-α method for integrating the filtered Navier-Stokes equations with a stabilized finite element method. *Computer Methods in Applied Mechanics and Engineering*, 190:305–319, 2000.
[97] M. R. Hestenes. Multiplier and gradient methods. *Journal of Optimization Theory and Applications*, 4(5):303–320, 1969.
[98] M. J. D. Powell. A method for nonlinear constraints in minimization problems. In R. Fletcher, editor, *Optimization*, pages 283–298. Academic Press, New York, 1969.
[99] H. Uzawa and K. J. Arrow. Iterative methods for concave programming. In *Preference, production, and capital*, pages 135–148. Cambridge University Press, 1989. Cambridge Books Online.
[100] C. Bacuta. A unified approach for Uzawa algorithms. *SIAM Journal on Numerical Analysis*, 44(6):2633–2649, 2006.
[101] S. Court, M. Fournié, and A. Lozinski. A fictitious domain approach for the Stokes problem based on the extended finite element method. *International Journal for Numerical Methods in Fluids*, 74(2):73–99, 2014.
[102] Y. Bazilevs, K. Takizawa, and T. E. Tezduyar. *Computational Fluid–Structure Interaction: Methods and Applications*. Wiley, Chichester, 2013.
[103] E. H. van Brummelen. Added mass effects of compressible and incompressible flows in fluid–structure interaction. *Journal of Applied Mechanics*, 76:021206, 2009.
[104] H.-G. Roos, M. Stynes, and L. Tobiska. *Numerical Methods for Singularly Perturbed Differential Equations. Convection–Diffusion and Flow Problems*. Springer, 1996.
[105] C. Hesch, A. J. Gil, A. Arranz Carreño, and J. Bonet. On continuum immersed strategies for fluid-structure interaction. *Computer Methods in Applied Mechanics and Engineering*, 247-248:51–64, 2012.
[106] A.J. Gil, A. Arranz Carreño, J. Bonet, and O. Hassan. An enhanced immersed structural potential method for fluid–structure interaction. *Journal of Computational Physics*, 250:178–205, 2013.
[107] T. Kenner. The measurement of blood density and its meaning. *Basic Research in Cardiology*, 84(2):111–124, 1989.
[108] R. Rosencranz and S. A. Bogen. Clinical laboratory measurement of serum, plasma, and blood viscosity. *American Journal of Clinical Pathology*, 125:S78–S86, 2006.

[109] H. Hasimoto. On the flow of a viscous fluid past a thin screen at small Reynolds numbers. *Journal of the Physical Society of Japan*, 13(6):633–639, 1958.

[110] C. H. Yap, N. Saikrishnan, G. Tamilselvan, and A. P. Yoganathan. Experimental technique of measuring dynamic fluid shear stress on the aortic surface of the aortic valve leaflet. *Journal of Biomechanical Engineering*, 133(6):061007, 2011.

[111] Y. Bazilevs, J. R. Gohean, T. J. R. Hughes, R. D. Moser, and Y. Zhang. Patient-specific isogeometric fluid–structure interaction analysis of thoracic aortic blood flow due to implantation of the Jarvik 2000 left ventricular assist device. *Computer Methods in Applied Mechanics and Engineering*, 198:3534–3550, 2009.

[112] M. Esmaily-Moghadam, Y. Bazilevs, T.-Y. Hsia, I. E. Vignon-Clementel, A. L. Marsden, and Modeling of Congenital Hearts Alliance (MOCHA). A comparison of outlet boundary treatments for prevention of backflow divergence with relevance to blood flow simulations. *Computational Mechanics*, 48:277–291, 2011.

[113] N. Westerhof, J.-W. Lankhaar, and B. E. Westerhof. The arterial Windkessel. *Medical & Biological Engineering & Computing*, 47:131–141, 2009.

[114] T. J. R. Hughes, W. K. Liu, and A. Brooks. Finite element analysis of incompressible viscous flows by the penalty function formulation. *Journal of Computational Physics*, 30(1):1–60, 1979.